1

Incorporation Mechanism and Functional Properties of Ce-Doped $BaTiO_3$ Ceramics Derived from Nanopowders Prepared by the Modified Pechini Method

Adelina-Carmen Ianculescu[1], Daniela C. Berger[2], Catalina A. Vasilescu[1,3], Marius Olariu[4], Bogdan S. Vasile[1], Lavinia P. Curecheriu[5], Andreja Gajović[6], and Roxana Truşcă[7]

[1]Department of Oxide Materials Science and Engineering, "Politehnica" University of Bucharest, Romania
[2]Department of Inorganic Chemistry, Physical-Chemistry and Electrochemistry, "Politehnica" University of Bucharest, Romania
[3]National Institute for Lasers, Plasma and Radiation Physics, Romania
[4]Department of Electrical Measurements and Materials, Technical University Gh. Asachi Iasi, Romania
[5]Department of Physics , "Alexandru Ioan Cuza" University, Romania
[6]Molecular Physics Laboratory, Institute Rudjer Boskovic, Croatia
[7]S.C. METAV – Research and Development Bucharest, Romania

1.1 Why Cerium-Doped $BaTiO_3$?

Donor-doped $BaTiO_3$ ceramics show very high endurance under DC field stress and a Curie temperature shift towards lower temperatures without flattening the permittivity

Nanoscale Ferroelectrics and Multiferroics: Key Processing and Characterization Issues, and Nanoscale Effects, First Edition. Edited by Miguel Algueró, J. Marty Gregg, and Liliana Mitoseriu.

maximum, as the solute concentration increases within the solubility range [1,2]. Regarding the microstructure, above a critical donor dopant content of ∼0.5 at% (also corresponding to an abrupt increase of the electrical resistivity), a strong grain growth inhibition known as a "grain growth anomaly" was observed [3–6]. For these reasons, donor-doped $BaTiO_3$ is suitable for the manufacture of multilayer capacitors with thin dielectric layers for applications as decoupling signals and high- and low-pass filters [1].

Due to its variable valence, cerium is a versatile solute for $BaTiO_3$. Therefore, the literature data regarding the oxidation state of cerium incorporated in a $BaTiO_3$ lattice seemed initially rather contradictory. Earlier, Kolar et al. reported a solubility of 18–20 mol% of CeO_2 incorporated as Ce^{4+} on Ti sites of $BaTiO_3$ [7]. Contrary to this result, Roth et al. [8] indicated the presence of Ce^{3+} in stable crystalline oxide phases (titanates, tantalates, and niobates), even if the cerium source was CeO_2 and sintering was carried out under an oxidizing atmosphere. Consistent with this view, Itakura et al. [9] found aliovalent substitution of Ba^{2+} by Ce^{3+} in $BaTiO_3$, induced by the close values of the ionic radii of these species in dodecahedral coordination ($r(Ba^{2+}) = 1.61$ Å, $r(Ce^{3+}) = 1.34$ Å). The incorporation of Ce^{3+} ions on Ti^{4+} sites as acceptors and the integration of Ce^{4+} on Ba^{2+} sites are very unlikely because of the high mismatch in ionic radius values of the substituting and substituted species ($r(Ti^{4+}) = 0.605$ Å and $r(Ce^{3+}) = 1.01$ Å for CN = 6; $r(Ba^{2+}) = 1.61$ Å and $r(Ce^{4+}) = 1.14$ Å for CN = 12). Later, some works of Hennings et al. [1], Makovec et al. [10], and Hwang and Han [11, 12] reconciled these apparent contradictory results. They showed that cerium may be incorporated either as Ce^{4+} on Ti^{4+} sites with the formation of homovalent $BaT_{1-y}Ce_yO_3$ solid solution or as Ce^{3+} on Ba^{2+} sites acting as donor dopant, or simultaneously as both Ce^{3+} on *A* sites and Ce^{4+} on *B* sites of the ABO_3 perovskite lattice, depending on the starting composition and oxygen partial pressure [1, 11, 13].

Based on the phase diagram of the $BaO–TiO_2–CeO_2$ system [14], the exhaustive study of Makovec et al. [10] showed that the starting Ba/Ti ratio plays a decisive role on the oxidation state of cerium, as well as on its solubility and lattice site occupancy into the host $BaTiO_3$ lattice. Thus, they concluded that: (i) for a Ba/Ti > 1 (CeO_2 is added to $BaTiO_3$ together with an excess amount of BaO), cerium is preferentially homovalently incorporated as Ce^{4+} on titanium sites and this solid solution extends along the $BaTiO_3–BaCeO_3$ tie line of the ternary $BaO–TiO_2–CeO_2$ system; (ii) for Ba/Ti < 1 (CeO_2 is added to $BaTiO_3$ with an excess amount of TiO_2), cerium is reduced and enters predominately as Ce^{3+} at barium sites acting as donor dopant; and (iii) for Ba/Ti = 1 (no excess of BaO or TiO_2), cerium is most likely incorporated both as Ce^{3+} at Ba sites and as Ce^{4+} at Ti sites in the ratio 3:4 and the solid solution extends on the tie-line $BaTiO_3–CeO_2$.

For Ba/Ti < 1, when cerium is entirely integrated as Ce^{3+} at Ba sites, several compensation mechanisms were proposed for the positive effective extracharge induced by the donor dopant. It is well known that the donor charge compensation mechanism is strongly dependent on several factors, such as partial pressure of oxygen in a firing atmosphere, sintering temperature, and donor concentration in the $BaTiO_3$ lattice [10, 15].

When sintering is carried out in air at high temperatures (above 1400 °C), the ceramics with a Ce^{3+} concentration below the critical value of 0.5 at% ($x < 0.005$) are described by the formula $Ba_{1-x}Ce^{\bullet}_xTi_{1-x}Ti'_xO_3$ (or shortly $Ba_{1-x}Ce_xTiO_3$). These samples exhibit a dark gray colour and semiconducting behaviour, as the result of an electronic compensation of the donor extracharge. This kind of mechanism involves the formation of reduced titanium

species, which act as acceptors and whose concentration is equal to the concentration of the donor dopant, that is $[Ce^{\bullet}] = [Ti']$. According to the Kröger–Vink notation [16] it can be described by:

$$2CeO_2 + 2TiO_2 \rightarrow 2Ce^{\bullet}_{Ba} + 2Ti^{\times}_{Ti} + 6O^{\times}_{O} + O_2(g) + 2e' \tag{1.1}$$

At a higher cerium content (>0.5 at%) ceramics sintered in air have reddish colour and are highly electrically insulating, which means that no electrons are available for conduction and, therefore, intrinsic effectively negatively charged defects as cation vacancies or interstitial anions are required for the compensation of the effective positive charge induced by the donor dopant.

Based on their calculations on defect energetics in barium titanate using computer simulation techniques, it was found [17] that interstitial incorporation of anions into the perovskite lattice, according to the theoretical formula $Ba_{1-x}Ce_xTiO_{3+x/2}$, where $[Ce^{\bullet}] = 2[O''_i]$, as described by the following quation, is very unlikely to take place because of the high packing density of this structure:

$$2CeO_2 + 2TiO_2 \rightarrow 2Ce^{\bullet}_{Ba} + 2Ti^{\times}_{Ti} + 6O^{\times}_{O} + O''_i + \frac{1}{2}O_2(g) \tag{1.2}$$

In some perovskite systems, such as doped $SrTiO_3$ and doped $PbTiO_3$, the donor compensation involves the formation of vacancies on the *A* sites of the perovskite lattice [18, 19]. In the case of Ce-doped $BaTiO_3$, if $Ce^{\bullet}$donors on Ba sites were to be entirely compensated by barium vacancies, then, according to the following equation, a ratio of co-additives $TiO_2/CeO_2 = 3{:}2$ relative to $BaTiO_3$ would be necessary to form a single-phase perovskite described by the formula $Ba_{1-3x/2}Ce_xTiO_3$ (where $[Ce^{\bullet}] = 2[V''_{Ba}]$):

$$2CeO_2 + 3TiO_2 \rightarrow 2Ce^{\bullet} + V''_{Ba} + 3Ti^{\times}_{Ti} + 9O^{\times}_{O} + \frac{1}{2}O_2(g) \tag{1.3}$$

Another assumption considers the formation of an equal number of barium and titanium vacancies for the compensation of donor extracharge. If this mechanism involving the co-additives ratio $TiO_2/CeO_2 = 1{:}1$ is valid, then a single-phase perovskite with the nominal formula $Ba_{1-7x/6}Ce_xTi_{1-x/6}O_3$ (where $[Ce^{\bullet}] = 2[V''_{Ba}] + 4[V''''_{Ti}]$) would be formed, according to:

$$6CeO_2 + 6TiO_2 \rightarrow 6Ce^{\bullet}_{Ba} + 6Ti^{\times}_{Ti} + V''_{Ba} + V''''_{Ti} + 21O^{\times}_{O} + \frac{3}{2}O_2(g) \tag{1.4}$$

The experimental data of Hennings et al. [1], who reported the preparation and properties of Ce-doped $BaTiO_3$ ceramics with various Ti/Ce ratios ($0 \leq Ti/Ce \leq 1.5$), showed that, actually, segregation of a Ti-rich second phase already occurred for the molar ratio $TiO_2/CeO_2 \cong 1$. Therefore, their results do not sustain the compensation mechanisms expressed by Equations (1.2) and (1.3). Consistent with this view, based on X-ray diffraction (XRD) and scanning electron microscopy (SEM), investigations corroborated with quantitative wavelength dispersive spectroscopy–electron probe microanalysis (WDS/EPMA), Makovec et al. [10] also showed that the compensation via double-ionized barium vacancy (Equation (1.3)) can be excluded. Similar to Hennings et al. [1], they found that when cerium is entirely incorporated as Ce^{3+} on Ba sites, the most likely compensation mechanism involves the generation of tetraionized titanium vacancies. This means that, for

a monophasic composition described by the nominal formula $Ba_{1-x}Ce_xTi_{1-x/4}O_3$, a co-additives ratio $TiO_2/CeO_2 = 3{:}4$ is required, according to:

$$4CeO_2 + 3TiO_2 \rightarrow 4Ce^{\bullet}_{Ba} + 3Ti^{\times}_{Ti} + V''''_{Ti} + 12O^{\times}_{O} + O_2(g) \tag{1.5}$$

Even if earlier double-ionized barium vacancies were considered to be the most likely charge compensating defects [20], later experimental data and theoretical calculations [15, 17, 21] sustained the assertion of Jonker and Havinga [22] and converged to the conclusion that tetra-ionized titanium vacancies are the preferred defects for compensation of donors in $BaTiO_3$ systems.

However, some recent works concerning the characteristics of donor-doped $BaTiO_3$ and $(Ba,Sr)TiO_3$ ceramics [23, 24] do not exclude the conclusion that the compensation mechanism via mixed cation vacancies (equal amounts of barium double-ionized and titanium tetra-ionized vacancies) might take place in certain processing conditions. Even for Ce-doped $BaTiO_3$, the study of Hwang and Han [12], based on the equilibrium electrical conductivity of the ceramics corresponding to the nominal formula $Ba_{1-x}Ce_xTiO_3$, which involves equimolar amounts of TiO_2 and CeO_2 admixtures, proposed the defect model including both Ba and Ti vacancies as compensating defects for $Ce^{\bullet}_{Ba}$, according to Equation (1.4). It is worthy to mention that XRD and SEM analyses used in a previous study of the same authors [11], while investigating $Ba_{1-x}Ce_xTiO_3$ ceramics sintered in air, were not able to emphasize, in the solubility range, the presence of any secondary phases as CeO_2- or TiO_2-rich compounds, which normally should be identified if compensation mechanisms via exclusive formation of double-ionized barium vacancies or of tetra-ionized titanium vacancies would be valid. According to the following modified equations of (1.3) and (1.5), for $TiO_2/CeO_2 = 1{:}1$:

$$3CeO_2 + 3TiO_2 \rightarrow 2Ce^{\bullet} + V''_{Ba} + 3Ti^{\times}_{Ti} + 9O^{\times}_{O} + CeO_2 + \frac{1}{2}O_2(g) \tag{1.3'}$$

$$4CeO_2 + 4TiO_2 \rightarrow 4Ce^{\bullet}_{Ba} + 3Ti^{\times}_{Ti} + V''''_{Ti} + 12O^{\times}_{O} + TiO_2 + O_2(g) \tag{1.5'}$$

From this point of view, Makovec et al. [10] revealed aspects concerning the defect chemistry in Ce-doped $BaTiO_3$ solid solutions placed on a hypothetical tie-line between $BaTiO_3$ and the composition corresponding to the ratio $TiO_2/CeO_2 = 1$ only for ceramics sintered in a reducing atmosphere. Unfortunately, no data regarding the phase composition, microstructure, and defect chemistry of similar ceramics sintered in air were reported. Consequently, the compensation mechanism in some Ce-doped $BaTiO_3$ ceramics sintered in air when cerium is dissolved as Ce^{3+} at barium sites is still under debate.

Some authors showed that the type of compensating defects in donor-doped $BaTiO_3$ depends on several factors, such as the type of solute, its lattice site occupancy, stoichiometry (A/B ratio), and sintering temperature [22, 23].

Not only the compensation mechanism but also the solubility limit of cerium into the $BaTiO_3$ lattice is expected to be influenced by the incorporation mechanism and A/B ratio. For $BaTi_{1-x}Ce_xO_3$ ceramics prepared by solid state and sintered in air at 1350 °C for 5 days, the solubility extends up to a Ce^{4+} concentration of ∼35 mol% [10], which is very close to the value of 33 mol% found by Ang et al. [25] for samples prepared by the same method and sintered at a higher temperature (1540 °C) for a much shorter time of 6 hours only. For

$Ba_{1-x}Ce_xTiO_3$ ceramics, a solubility limit for Ce^{3+} of 7 mol% for ceramics prepared by the Pechini method and sintered in air at 1350 °C for 5 hours was reported [11]. On the other hand, for the *A*-site cerium-doped $BaTiO_3$ with built-in titanium vacancies, described by the formula $Ba_{1-x}Ce_xTi_{1-x/4}V''''_{x/4}O_3$, Hennings et al. [1], Makovec et al. [10], and Jing et al. [26] found the same solubility limit of 8 mol%, for ceramics prepared by solid state and sintered in air, at temperatures above 1350 °C. The solubility of Ce^{3+} on Ba sites strongly decreases with sintering temperature, so that a solubility limit of only 4 mol% was found for ceramics prepared by the same route, but sintered at 1200 °C [10].

The *A*-site and *B*-site cerium-doped barium titanate ceramics also show different electrical behavior. Thus, according to the latest literature data for $BaTi_{1-y}Ce_yO_3$ solid solutions, the Curie temperature shifts slowly towards lower temperatures when increasing Ce^{4+} content, with a rate of about –7 °C/at% [27] or –3 °C/at% [28]. Besides, for a substitution degree $y > 0.1$, the increase of the solute content in $BaTi_{1-y}Ce_yO_3$ ceramics induces a gradual change in the electrical behavior, from a classic ferroelectric towards a relaxor [29,30]. Similarly, for the *A*-site cerium-doped solid solutions, a much faster linear decrease of the Curie temperature with the increase of Ce^{3+} content was found, with a rate of the Curie temperature decrease of –18 °C/at% [26] for $Ba_{1-x}Ce_xTi_{1-x/4}V''''_{x/4}O_3$, while values of –21 °C/at% [11, 31] and –22.5 °C/at% [32] were found for $Ba_{1-x}Ce_xTiO_3$ ceramics.

A specific feature of the ferroelectric–paraelectric phase transition in *A*-site cerium-doped $BaTiO_3$ ceramics sintered above 1350 °C is that the permittivity maxima remain very sharp, proving a typical ferroelectric behavior for all the compositions in the solubility limit [1, 11, 12, 26, 31]. Only Yasmin et al. [32] reported diffuse phase transitions and lower values of dielectric maxima ($\varepsilon_r < 3000$) for their fine-grained $Ba_{1-x}Ce_xTiO_3$ ($0 \leq x \leq 0.04$) ceramics sintered in air at 1200 °C/4 h.

Taking into account the fact that almost similar electrical behavior was reported for ceramics sintered in air, with identical Ce^{3+} content incorporated on Ba sites but with dissimilar (Ba+Ce)/Ti ratios and processed by different routes in different sintering conditions, we concluded that a systematic study concerning the influence of the cation stoichiometry (*A*/*B* ratio) on the dielectric characteristics of the Ce^{3+}-doped $BaTiO_3$ ceramics prepared by the same processing technique and sintered in air at different temperatures deserves more attention. For this purpose, we have chosen two compositions, with different *A*/*B* ratios, but both with the same cerium content, that is 5 at% Ce^{3+} incorporated on Ba sites into a $BaTiO_3$ lattice. Several works reported a shift of the Curie temperature value near to 25 °C [1, 11, 12, 31] for this Ce^{3+} concentration and, consequently, this kind of composition provides promising candidates for room temperature ceramic capacitor applications.

Various methods such as the solid-state reaction [1, 26, 32], sol–gel [33] and the Pechini method [11,12] have been utilized for preparing Ce^{3+}-doped $BaTiO_3$. The modified Pechini process is known as an excellent preparation technique for controlling stoichiometry and homogeneity of the oxide materials [34] and it was employed for the present study.

In the present work, 5% Ce-doped $BaTiO_3$ nanopowders were prepared by a modified Pechini method. Two types of solid solutions were comparatively investigated: (i) the first one is similar to the composition investigated by Hwang and Han [11, 12], which corresponds to the nominal formula $Ba_{0.95}Ce_{0.05}TiO_3$ (i.e. a cation ratio (Ba + Ce)/Ti = 1) and the lack of any compensating ionic defects, and (ii) one described by the nominal formula $Ba_{0.95}Ce_{0.05}Ti_{0.9875}(V''''_{Ti})_{0.0125}O_3$ ((Ba + Ce)/Ti ≅ 1.0127), which has the adjusted

concentration of built-in titanium vacancies, as studied by Jing et al. [26]. Actually, for the first nominal composition $Ba_{0.95}Ce_{0.05}TiO_3$, taking into account the high cerium content (with an order of magnitude higher than the critical concentration), which excludes the charge compensation via the electronic mechanism, if a single-phase composition is assumed, the correct nominal formula would be $Ba_{0.95}Ce_{0.05}TiO_{3.025}$, which involves a charge compensation by oxygen ions on interstitial sites, according to Equation (1.2). Since this compensation mechanism is very unlikely, segregation of secondary phases should occur in this case. Therefore, we considered that we can refer to this composition as being described by the nominal formula $Ba_{0.95}Ce_{0.05}TiO_3$, as in other similar works concerning highly Ce^{3+}-doped $BaTiO_3$ [11, 12, 31, 32].

1.2 Sample Preparation, Phase and Nano/Microstructural Characterization

1.2.1 Powders

1.2.1.1 Powder Synthesis Procedure

Nanopowders with nominal compositions, $Ba_{0.95}Ce_{0.05}TiO_3$ and $Ba_{0.95}Ce_{0.05}Ti_{0.9875}(V_{Ti}'''')_{0.0125}O_3$, were prepared via a modified Pechini method [15] from titanium isopropoxide ($Ti(iOC_3H_7)_4$, Merck, Germany), cerium(III) carbonate ($Ce_2(CO_3)_3{\cdot}xH_2O$, Acros Organics, US), barium carbonate (Merck, Germany), citric acid (99.5% GR grade, Merck, Germany) as chelating agent and ethylene glycol (99.5% GR grade, Merck, Germany) as both solvent and polyesterification agent.

A solution of 5 mL of titanium isopropoxide was added to a solution previously obtained by dissolving under heating 5 g of citric acid in 20 mL of ethylene glycol. This reaction mixture was heated at 80 °C/2 h on a plate under magnetic stirring. Separately, for each nominal composition, two different solutions of barium citrate and cerium citrate were prepared. Barium citrate solutions were obtained by dissolving in 20 mL 4 *M* aqueous citric acid solution of 3.1864 g and 3.2267 g $BaCO_3$, for the preparation of the Ce–$BaTiO_3$ powders. Cerium citrate solutions were obtained by dissolving in 5 mL 4 *M* aqueous citric acid solution of 0.2415 g and 0.2445 g $Ce_2(CO_3)_3{\cdot}xH_2O$, respectively. In both cases barium citrate and cerium citrate solutions were added to the yellowish solution containing titanium ions. The resulting colourless solutions were kept under magnetic stirring at 80 °C/1 h. During this process, the solutions became increasingly viscous until yellow gels were produced. These gels were thermally treated on a sand bath at 135 °C/25 h (without stirring) for polyesterification reaction and water removal. The resulting orange-brown glassy resins were burnt out in air, at 400 °C/2 h in an electric furnace, to remove the organic matter. During the thermal treatment, the volume of resins has gradually increased, until foam-like, black residues or the so-called "precursors", were formed. After cooling, the residues were ground, so that fine powders, with a vitreous aspect, were obtained. The final thermal treatment at 900 °C/2 h was carried out to obtain yellowish Ce–$BaTiO_3$ oxide nanopowders.

1.2.1.2 Phase Composition and Structure

X-ray diffraction measurements at room temperature were performed with a Shimadzu XRD 6000 diffractometer (SHIMADZU, Kyoto, Japan) using Ni-filtered CuKα

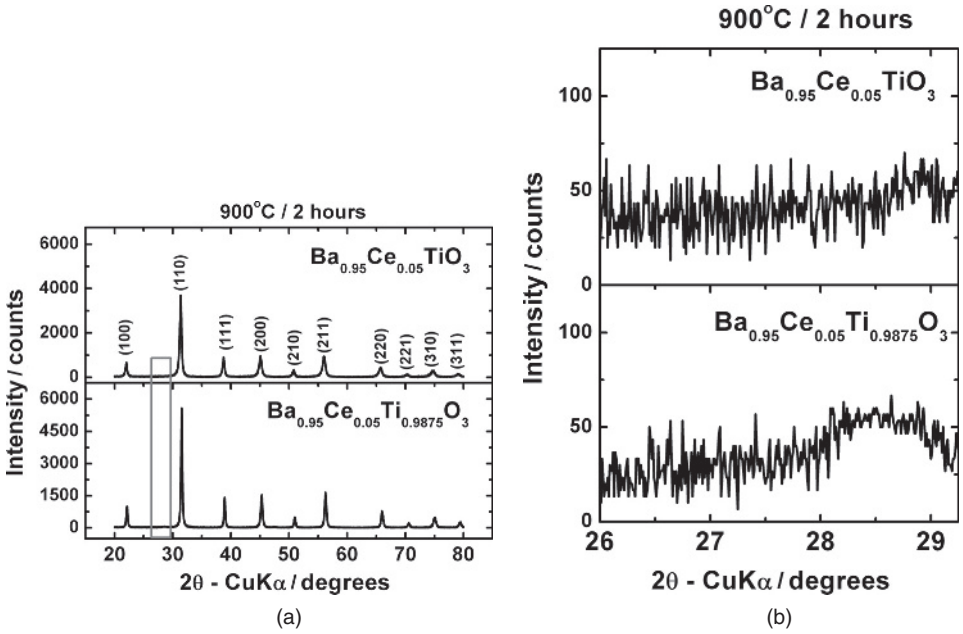

Figure 1.1 *(a) Room temperature XRD patterns of 5% Ce-doped $BaTiO_3$ powders thermally treated at 900 °C/2 h and (b) detail (rectangle in Figure 1.1(a)) of the region corresponding to diffraction angles 2θ =26–29.25°*

radiation (λ = 1.5418 Å), with a scan step of 0.02° and a counting time of 1 s/step, for $2\theta \in (20 - 80)°$.

The XRD patterns obtained for the powders thermally treated at 900 °C/2 h and slowly cooled at room temperature show the presence of a well-crystallized perovskite phase, identified by the main diffraction reflections specific to the $BaTiO_3$ structure, for both compositions (Figure 1.1(a)). The lack of visible, well-defined peaks corresponding to some secondary phases seems to indicate monophasic compositions. A careful examination of the region corresponding to diffraction angles of 2θ = 26–29.25° in the XRD pattern of the $Ba_{0.95}Ce_{0.05}Ti_{0.9875}(V_{Ti}^{''''})_{0.0125}O_3$ powder (Figure 1.1(b)) shows a very small, flattened feature centred around 2θ = 28.5°, which might correspond to small amounts of CeO_2 and polytitanates secondary phases, which proves that dopant was not yet entirely incorporated in the perovskite lattice. We cannot exclude the presence of these secondary phases also in the $Ba_{0.95}Ce_{0.05}TiO_3$ powders, but most likely they are below the detection limit.

Based on XRD data, structural characteristics as lattice constants and average crystallite size values were also calculated. Parameters to define the position, magnitude, shape, and integral breadth or full width at half maximum (FWHM) of the profile of the individual peaks are obtained using the pattern fitting and profile analysis of the original X-ray 5.0 program. The lattice constants calculation is based on the least squares procedure (LSP) using the linear multiple regressions for several XRD lines, depending on the unit cell symmetry. To deconvolute size-*D* and strain-*S* broadening from the XRD patterns of the powders, the multiple line analysis and integral breadth methods applied to the observed profiles

Table 1.1 *Structural parameters of 5% Ce–$BaTiO_3$ powders thermally treated at 900 °C/2 h*

Structural parameters	Composition		
	$Ba_{0.95}Ce_{0.05}TiO_3$		$Ba_{0.95}Ce_{0.05}Ti_{0.9875}O_3$
Symmetry	Cubic	Tetragonal	Cubic
a (Å)	4.0265(32)	4.0182(32)	4.0091(22)
c (Å)	4.0265(32)	4.0529(54)	4.0091(22)
c/a	1.000	1.0086(21)	1.000
V (Å3)	65.28(18)	65.44(19)	64.44(11)
<*D*> (Å)	741(39)	766(65)	792(78)
<*S*> × 10^{-3}	0.26(3)	0.40(4)	0.10(2)

(properly approximated with Pearson's VII analytic functions) were used. Thus, analysis of the diffraction peak positions and profiles emphasizes a single cubic form in the sample with built-in compensating defects, whereas a mixture of cubic and tetragonal modifications was found in the $Ba_{0.95}Ce_{0.05}TiO_3$ powders. Calculation of structural parameters indicates that the presence of the titanium vacancies seems to favor the cubic modification, by inducing the shrinkage of the unit cell by decreasing the lattice constant (Table 1.1). Values corresponding to the average crystallite size, <*D*>, and internal microstrains, <*S*>, were also listed in Table 1.1. A slightly higher value of the crystallite size and lower internal microstrains were found for the powder with built-in Ti vacancies.

1.2.1.3 Powder Morphology

In order to analyze powder morphology and crystallinity degree, TEM (transmission electron microscopy) and HRTEM (high-resolution TEM) coupled with SAED (surface area electron diffraction) investigations were performed using a high-resolution transmission electron Tecnai G^2 F30 S-TWIN microscope (FEI Co., The Netherlands).

TEM investigations revealed uniform particles with an average size of 76 nm for the $Ba_{0.95}Ce_{0.05}TiO_3$ powder and 81 nm for the $Ba_{0.95}Ce_{0.05}Ti_{0.9875}(V''''_{Ti})_{0.0125}O_3$ powder (Figure1.2(a) and 1.3(a)). This estimation is in good agreement with the average crystallite size calculated from XRD data and demonstrates the single-crystal nature of the particles of both compositions. The $Ba_{0.95}Ce_{0.05}TiO_3$ powder consists of isolated particles with polyhedral shape and well-defined edges, which are joined at sharp angles (Figure 1.2(a)), in comparison with the more rounded particles, exhibiting a higher agglomeration tendency, corresponding to the $Ba_{0.95}Ce_{0.05}Ti_{0.9875}(V''''_{Ti})_{0.0125}O_3$ composition (Figure 1.3(a)). The high crystallinity degree of the particles of both powders was emphasized by the highly ordered fringes corresponding to the crystalline planes (111), (211), and (200) in the HRTEM images of Figure 1.2(b) and 1.3(b), respectively.

It is worthy of mention that no particles with dissimilar morphologies, which might indicate the presence of some secondary phases, were detected by TEM analyses. Indexing of HRTEM images taken on several particles at the maximum magnification of the microscope, as well as indexing of selected surface area electron diffraction (SAED) patterns

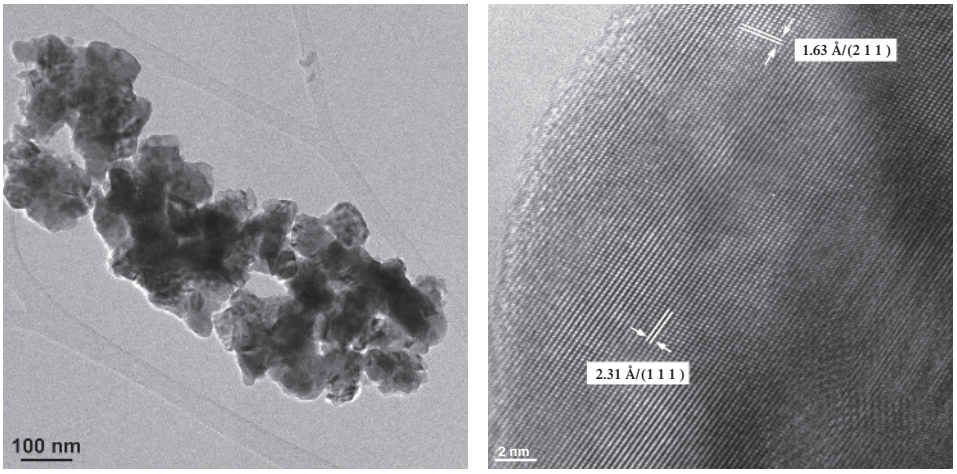

(a) (b)

Figure 1.2 *(a) TEM and (b) HRTEM images of $Ba_{0.95}Ce_{0.05}TiO_3$ powder thermally treated at 900 °C/2 h*

corresponding to several non-agglomerated areas and individual particles did not show the presence of CeO_2 or of any barium- or titanium-rich secondary phase. Moreover, EDX investigations carried out on several individual particles did not reveal any significant deviation of the Ba/Ti ratio (which should appear in Ba- or Ti-rich secondary phases) relative to $BaTiO_3$. However, this is not surprising, since the identification of small amounts of secondary phases in powdered samples is a harder task than detecting them by SEM in bulk ceramics.

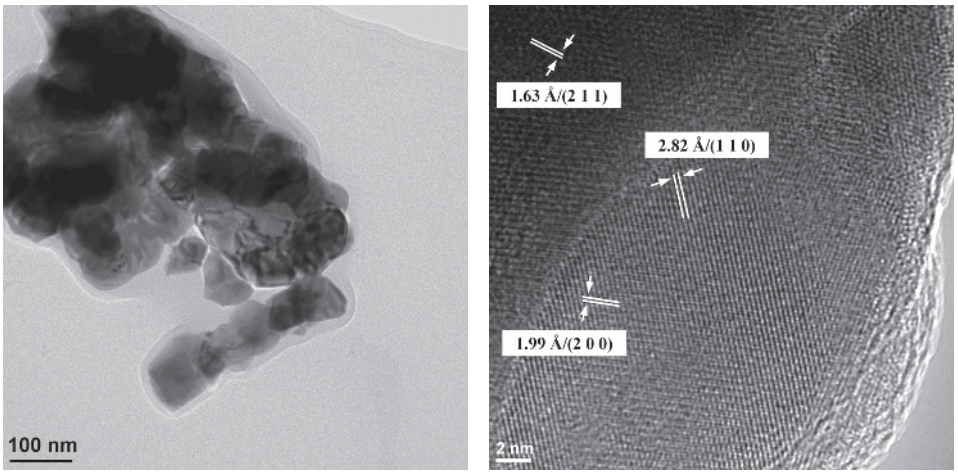

(a) (b)

Figure 1.3 *(a) TEM and (b) HRTEM images of $Ba_{0.95}Ce_{0.05}Ti_{0.9875}(V''''_{Ti})_{0.0125}O_3$ powder thermally treated at 900 °C/2 h*

1.2.2 Ceramics

1.2.2.1 Ceramics Preparation

The powders were uniaxially pressed into pellets (of 13 mm diameter and ∼2 mm thickness), using an organic binder (5% aqueous solution of polyvinyl alcohol). These pellets were sintered in air at temperatures of 1200 and 1300 °C, with a heating rate of 5 °C/min and a soaking time of 4 hours, and then they were slowly cooled down to room temperature at the normal cooling rate of the furnace.

Ceramic samples are denoted in the following as: A and B, representing specimens with the nominal composition $Ba_{0.95}Ce_{0.05}TiO_3$ sintered at 1200 and 1300 °C/4 h, respectively, while C and D refer to specimens with the nominal formula $Ba_{0.95}Ce_{0.05}Ti_{0.9875}(V_{Ti}'''')_{0.0125}O_3$ sintered in similar conditions. Ceramics A, B, and C exhibit a light-orange colour, while the ceramic D is intensely red.

1.2.2.2 Phase Composition and Structure

In order to check the phase purity in the ceramic samples, X-ray diffraction investigations were performed by means of an X'Pert Pro MPD diffractometer with a PIXcel detector (PANalytical, Almelo, The Netherlands), using the same radiation (Ni-filtered CuKα radiation), but with a scan step of 0.013° and a counting time of 150 s/step.

XRD patterns of both ceramics seem to indicate single-phase compositions, consisting of well-crystallized $BaTiO_3$ solid solutions, identified by the main reflections of the perovskite structure (Figure 1.4(a) and 1.5(a)). However, as in powders, the details (rectangles

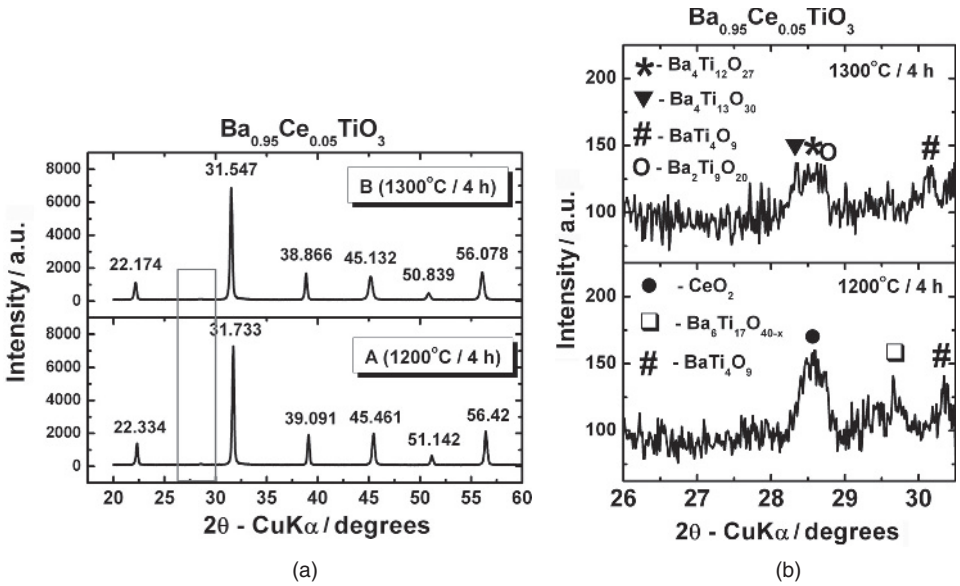

Figure 1.4 *(a) Room temperature XRD patterns of ceramics corresponding to the nominal formula $Ba_{0.95}Ce_{0.05}TiO_3$ sintered in air at 1200 °C/4 h (sample A) and 1300 °C/4 h (sample B), respectively; (b) detail (rectangle in Figure 1.4(a)) of the region corresponding to diffraction angles 2θ = 26–30.5°*

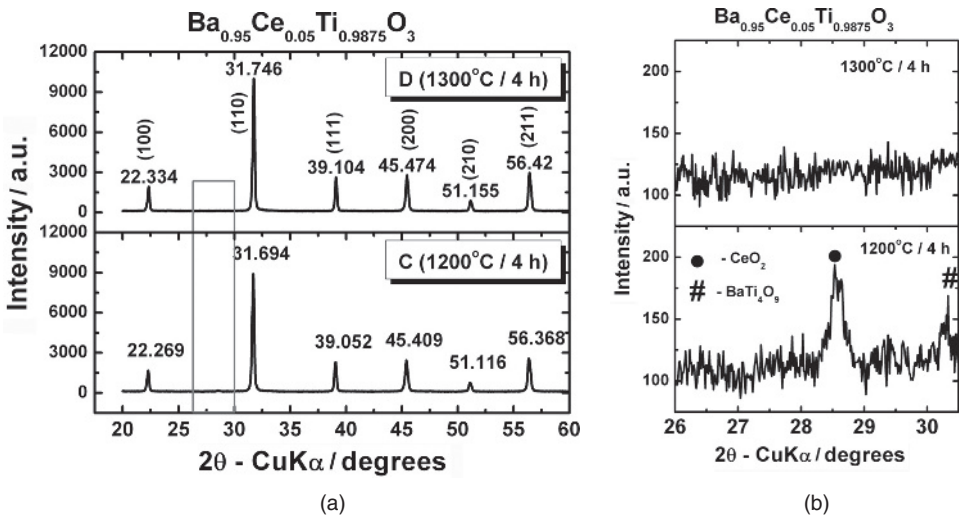

Figure 1.5 *Room temperature XRD patterns of ceramics corresponding to the $Ba_{0.95}Ce_{0.05}Ti_{0.9875}(V''''_{Ti})_{0.0125}O_3$ ceramic sintered in air at 1200 °C/4 h (sample A) and 1300 °C/4 h (sample B), respectively; (b) detail (rectangle in Figure 1.5(a)) of the region corresponding to diffraction angles $2\theta = 26–30.5°$*

in Figures 1.4(a) and 1.5(a)) of the region corresponding to diffraction angles $2\theta = 26–30.5°$ show the presence of small amounts of secondary phases (Figure 1.4(b) and 1.5(b)). Thus, for both ceramics sintered at 1200 °C, irrespective of the (Ba + Ce)/Ti ratio, CeO_2 (JCPDS file no. 43-1002) was identified by means of the main reflection (111) at $2\theta = 28.54°$. Typically, precipitation in solid solutions occurs at lower temperatures because of the reduced solid solubility of the dopant. As already mentioned, cerium, acting as a donor on Ba sites, exhibits a maximum solubility of only 4 at% Ce^{3+} on Ba sites at 1200 °C. Therefore, the Ce^{3+} concentration of 5 at% stipulated by the nominal compositions of our samples overpassed the solubility limit at 1200 °C, which might apparently explain the precipitation process. However, when the solubility limit is exceeded, Ce^{3+} should be precipitated and not Ce^{4+} [35]. Therefore, another explanation should be found for CeO_2 precipitation in the ceramic samples sintered at 1200 °C. According to the study of Makovec and Kolar [35], based on their HRTEM/SAED results on single phase Ce^{3+}-doped $BaTiO_3$ ceramics, internal partial oxidation of Ce^{3+} to Ce^{4+}, accompanied by heterogeneous precipitation of small amounts of fluorite CeO_2 and polytitanates in the perovskite matrix, takes place after annealing at higher temperatures of 1000–1100 °C. They demonstrated that this process is controlled by oxygen diffusion, which is strongly enhanced at the grain boundary regions and extended defects (subgrain boundaries and (111) twin boundaries) in comparison with oxygen diffusion in the perovskite lattice. The stoichiometry of the nominal compositions of Ce^{3+}–$BaTiO_3$ solid solutions demands that precipitation of CeO_2 be accompanied by precipitation of some TiO_2-rich secondary phases. Therefore, the partial reoxidation of Ce^{3+} induces the removal of Ce^{4+} ions together with Ti^{4+} ions in the atomic ratio Ce/Ti = 4/3, from the $Ba_{0.95}Ce_{0.05}Ti_{0.9875}(V''''_{Ti})_{0.0125}O_3$ solid solution. For the $Ba_{0.95}Ce_{0.05}TiO_3$ solid

solution, the amount of precipitated Ti-rich phases should be even larger (Ce/Ti = 1) by considering the lack of compensating defects.

Indeed, in Figure 1.4(b) one can observe that, beside CeO_2, small amounts of polytitanate phases consisting of a mixture of Ba_4TiO_9 (JCPDS file no. 77-1345) and $Ba_6Ti_{17}O_{40}$ (JCPDS file no. 43-0559) were identified for the $Ba_{0.95}Ce_{0.05}TiO_3$ ceramic sintered at 1200 °C/4 h. For the $Ba_{0.95}Ce_{0.05}Ti_{0.9875}(V_{Ti}^{''''})_{0.0125}O_3$ specimen sintered in the same conditions only Ba_4TiO_9 was detected (Figure 1.5(b)).

The segregation of CeO_2 in the grain boundary regions induces the incorporation of a lower amount of cerium solute in the perovskite matrix than one corresponding to $x = 0.05$, stipulated by the nominal formulae. Consequently, for the ceramic specimens sintered at 1200 °C, the lowering of Ce^{3+} content incorporated on Ba sites into the perovskite lattice should be reflected in the Curie temperature, which should exhibit a higher value than one of ∼25 °C, corresponding to the solid solution with 5 at% Ce^{3+} integrated on barium sites [1, 11, 12, 31]. Dielectric investigations shown later in Section 1.3 were aimed to clarify this aspect.

After sintering at 1300 °C, the ceramic corresponding to the nominal composition with built-in $V_{Ti}^{''''}$ seems to be single phase, whereas for the ceramic without compensating defects, small amount of polytitanate phases with a variable Ba/Ti ratio (Ba/Ti = 3–4.5) are still identified. These polytitanates might be $Ba_4Ti_{12}O_{27}$ (JCPDS file no. 04-011-4266), $Ba_4Ti_{13}O_{30}$ (JCPDS file no. 73-1188), Ba_4TiO_9 (JCPDS file no. 77-1565), and $Ba_2Ti_9O_{20}$ (JCPDS file no. 40-0405) (Figures 1.4(b) and 1.5(b)). This indicates that, as was expected, in $Ba_{0.95}Ce_{0.05}TiO_3$ ceramic, the excess of titanium (relative to the nominal formula corresponding to the most likely charge compensation mechanism) could not be fully accommodated in the perovskite lattice and, consequently, it was expelled as Ti-rich secondary phases. CeO_2 precipitate was not identified in the ceramic with built-in compensating defects sintered at 1300 °C, which means that the increase of sintering temperature no longer favours the internal reoxidation process of Ce^{3+} ions, at least for the $Ba_{0.95}Ce_{0.05}Ti_{0.9875}(V_{Ti}^{''''})_{0.0125}O_3$ composition. Therefore, in this case, the perovskite solid solution should present the same composition as one stipulated by the nominal formula. For the $Ba_{0.95}Ce_{0.05}TiO_3$ composition this assertion is difficult to sustain, since the main diffraction peak of the potential CeO_2 residual phase overlaps the main reflections of some polytitanate phases. Therefore, we concluded that an indubitable internal reoxidation process of Ce^{3+} involving CeO_2 precipitation takes place in the ceramics sintered at 1200 °C. Complementary investigations are required in order to establish what really happens with Ce^{3+} ions in the ceramics sintered at 1300 °C, especially in the one corresponding to the nominal formula $Ba_{0.95}Ce_{0.05}TiO_3$.

The structural parameter calculations based on the XRD data showed a significant decrease of the unit cell parameters and volume for the ceramic samples with built-in Ti vacancies, irrespective of the sintering temperature (Table 1.2).

For the ceramics sintered at 1200 °C, the evolution of the unit cell symmetry maintains the same tendency as in the precursor oxide powders, that is the composition with built-in compensating defects (C) favours the cubic modification, while the $Ba_{0.95}Ce_{0.005}TiO_3$ (A) sample consists of a mixture of tetragonal and cubic forms.

Concerning the specimens sintered at 1300 °C, a mixture consisting of a cubic major phase and a minor tetragonal modification was emphasized for the $Ba_{0.95}Ce_{0.05}Ti_{0.9875}(V_{Ti}^{''''})_{0.0125}O_3$ ceramic (D), whereas a pure tetragonal form was found for the

Table 1.2 *Structural parameters of 5% Ce–$BaTiO_3$ ceramics*

Structural parameters	Composition					
	$Ba_{0.95}Ce_{0.05}TiO_3$			$Ba_{0.95}Ce_{0.05}Ti_{0.9875}O_3$		
	A (1200 °C)		B (1300 °C)	C (1200 °C)	D (1300 °C)	
Symmetry	Cubic +	Tetragonal	Tetragonal	Cubic	Cubic +	Tetragonal
a (Å)	4.0155(13)	4.0067(19)	4.0239(11)	3.9974(4)	3.9721(24)	3.9878(7)
c (Å)	4.0155(13)	4.0173(44)	4.0465(26)	3.9974(4)	3.9721(24)	4.0006(9)
c/a	1.0000	1.0026(16)	1.0056(9)	1.0000	1.0000	1.0032(26)
V (Å^3)	64.74(6)	64.49(13)	65.52(8)	63.88(2)	62.67(11)	63.62(22)

$Ba_{0.95}Ce_{0.05}TiO_3$ sample (B). Fitting was carried out using JCPDS files no. 31-0174 for the cubic form and no. 05-0626 for the tetragonal form, respectively.

The presence of a mixture of two perovskite modifications (cubic and tetragonal) detected in some of the specimens might indicate the proximity of the ferroelectric–paraelectric phase transition close to room temperature, while the presence of a pure tetragonal form in the ceramic sample without built-in titanium vacancies and sintered at a higher temperature (B) seems to indicate a typical ferroelectric state.

In the case of $Ba_{0.95}Ce_{0.05}TiO_3$ specimens, higher values of lattice parameters were determined for the tetragonal form, when sintering was carried out at a higher temperature (1300 °C), while an opposite evolution against sintering temperature is indicated by the lattice parameter values corresponding to the major cubic phase of the $Ba_{0.95}Ce_{0.05}Ti_{0.9875}(V_{Ti}^{''''})_{0.0125}O_3$ sample. This latter evolution seems normal and is consistent with the slight shift of the main diffraction peaks of the perovskite phase towards higher values of the diffraction angle shown by the XRD pattern (Figure 1.5(a)). This shift, together with the lack of CeO_2 precipitate in the sample with built-in Ti vacancies sintered at 1300 °C seems to originate in an increasing amount of solute with a lower ionic radius incorporated on *A*-sites of the perovskite lattice, when the sintering temperature increased. Therefore, in the ceramic specimen sintered at 1300 °C, the whole cerium content stipulated by the nominal formula was incorporated as Ce^{3+} into the barium titanate lattice, in comparison with the sample with similar nominal composition sintered at 1200 °C. This latter sample should be in fact poorer in Ce^{3+}, taking into account the small amount of CeO_2 precipitate identified at the detection limit in its XRD pattern.

It remains to elucidate the unexpected shift of the diffraction peaks towards lower values of the diffraction angles (Figure 1.4(a)) and the significantly higher values of the lattice parameters for the sample described by the nominal formula $Ba_{0.95}Ce_{0.05}TiO_3$ sintered at 1300 °C, in comparison with those corresponding to the specimen with a similar nominal composition but sintered at 1200 °C (Table 1.2).

We also need to mention that in perovskite solid solutions sometimes the average cubic state can correspond at the local level to a non-centrosymmetric phase with a low distortion, close to the cubic one ("pseudocubic state") or to a mixture of such states. Therefore, dielectric investigations at different temperatures were performed to provide additional

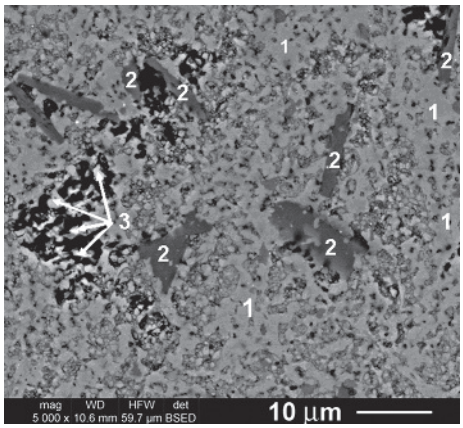
1
2
2
2
1
2
3
2
2
1
1
mag WD HFW det
5 000 x 10.6 mm 59.7 µm BSED
10 µm

(a)

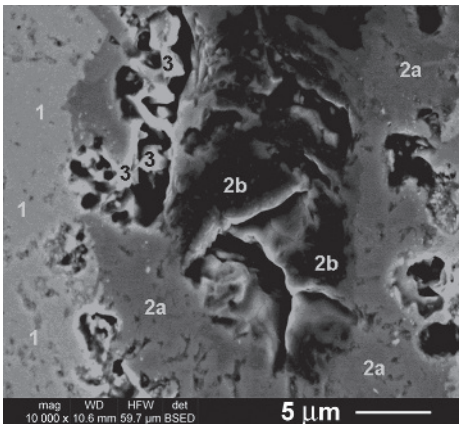
3
2a
1
3
3
2b
1
2b
2a
1
2a
mag WD HFW det
10 000 x 10.6 mm 59.7 µm BSED
5 µm

(b)

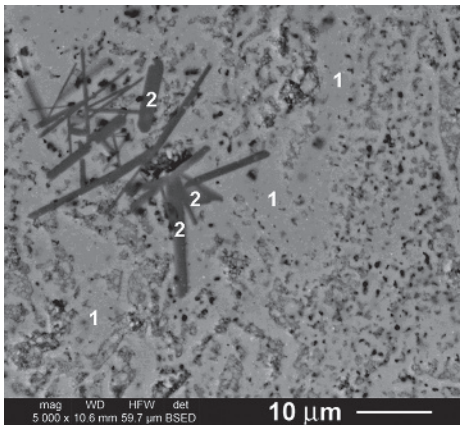
1
2
1
2
2
1
1
mag WD HFW det
5 000 x 10.6 mm 59.7 µm BSED
10 µm

(c)

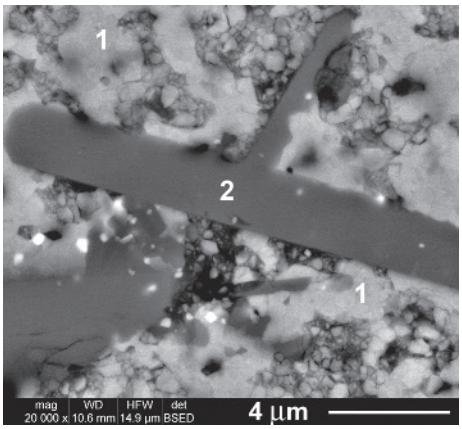
1
2
1
mag WD HFW det
20 000 x 10.6 mm 14.9 µm BSED
4 µm

(d)

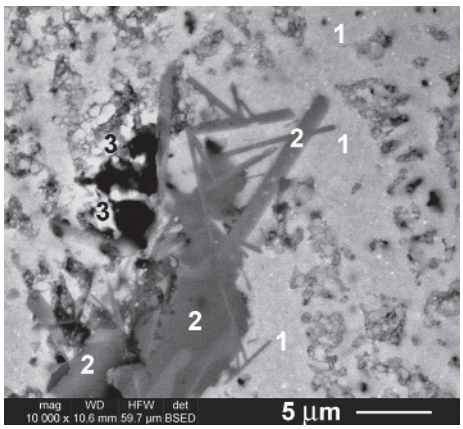
1
3
2
1
3
2
1
2
mag WD HFW det
10 000 x 10.6 mm 59.7 µm BSED
5 µm

(e)

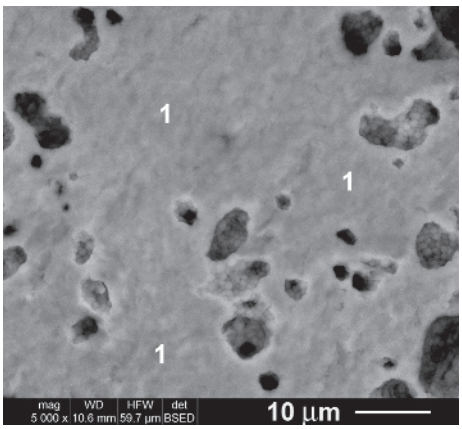
1
1
1
1
mag WD HFW det
5 000 x 10.6 mm 59.7 µm BSED
10 µm

(f)

information and to explain the structural features determined by means of the XRD data at room temperature.

1.2.2.3 Ceramics Microstructure

A high-resolution scanning electron microscope Quanta Inspect F (FEI Co., The Netherlands) with a field emission (FE gun SEM coupled with energy-dispersive X-ray spectroscopy (EDX)) was used to analyze the microstructure and the chemical composition of the ceramics. To search for possible existing secondary phases, FE-SEM investigations were carried out first in BSE (back-scattered electron) mode on polished sections. After subsequent thermal etching, microstructural features were examined by performing analyses in SE (secondary electron) mode. The average grain size was calculated using the OriginPro 8.5 software (statistics on column) by taking into account equivalent size measurements on ∼70 grains (from images of appropriate magnifications obtained from various microscopic fields) performed by means of the microscope software ImageJ. The relative density of the sintered ceramic pellets was calculated as the ratio between the apparent density measured by Archimedes' principle and the crystallographic (theoretical) density.

The FE-SEM image in BSE mode on a polished cross-section of the $Ba_{0.95}Ce_{0.05}TiO_3$ ceramic sintered at 1200 °C shows the presence of some dark-gray areas denoted 2, of various sizes and irregular shapes, but predominantly with an elongated aspect (i.e. fibrous, acicular and rod-like morphology), uniformly distributed in a light-gray matrix denoted 1 (Figure 1.6(a) and (b)). This indicates that titanium-rich secondary phases are formed in the whole matrix of perovskite grains. Such regions were observed in three of the four samples investigated here, that is both ceramics A and B corresponding to the nominal composition $Ba_{0.95}Ce_{0.05}TiO_3$, irrespective of sintering temperature, and the ceramic specimen C with built-in titanium vacancies sintered at 1200 °C. Small CeO_2 grains of bright-white color, denoted 3, were also identified in the ceramic samples A and C sintered at 1200 °C/4 h. Only ceramic D, with built-in Ti vacancies, sintered at 1300 °C, seems to be single phase. Figure 1.6(a) and (b) shows a general view indicating the distribution of phases and a detail of a region containing polytitanate phases with a variable Ba:Ti ratio (Ba:Ti ∼ 1:3–1:4), corresponding mainly to $Ba_6Ti_{17}O_{40}$ (denoted 2a) and $BaTi_4O_9$ (denoted 2b), in a $Ba_{0.95}Ce_{0.05}TiO_3$ sample (A) sintered at 1200 °C, while Figure 1.6(c) and (d) reveals a general view and a detail showing the elongated shape of an area specific to the secondary polytitanate phase with a Ba:Ti ratio ∼1:3 in ceramic sample B, with similar composition but sintered at 1300 °C. A distribution of phases similar to that indicated in Figure 1.6(a) was observed in ceramic sample C (Figure 1.6(e)), which corresponds to the

Figure 1.6 *FE-SEM images in the BSE mode on polished cross-sections of ceramics before thermal etching: (a) general view and (b) detail of sample A (without Ti vacancies and sintered at 1200 °C/4 hours), showing secondary phases denoted in accord with quantitative EDX analyses: (1) perovskite matrix; (2a) poly-titanate phase with a Ba:Ti ratio ∼1:3; (2b) polytitanate phase with a Ba:Ti ratio ∼1:4; (3) CeO_2; (c) general view and (d) detail of sample B (with similar composition, but sintered at 1300 °C/4 h), showing the predominantly elongated shape of poly-titanates areas; (e) detail of sample C (with built-in Ti vacancies sintered at 1200 °C/4 h) and (f) general view of the monophasic sample D (with built-in Ti vacancies sintered at 1300 °C/4 h)*

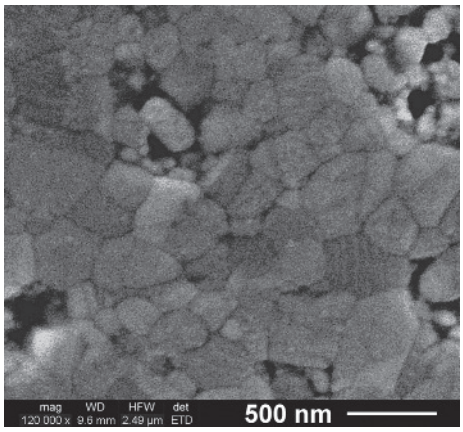
mag WD HFW det
120 000 x 9.6 mm 2.49 µm ETD
500 nm

(a)

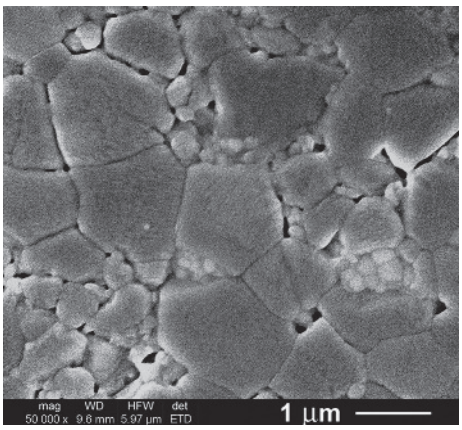
mag WD HFW det
50 000 x 9.6 mm 5.97 µm ETD
1 µm

(b)

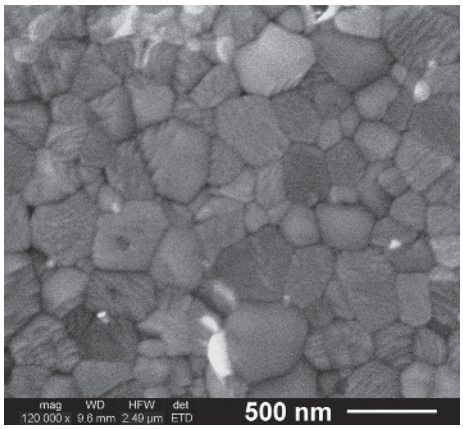
mag WD HFW det
120 000 x 9.6 mm 2.49 µm ETD
500 nm

(c)

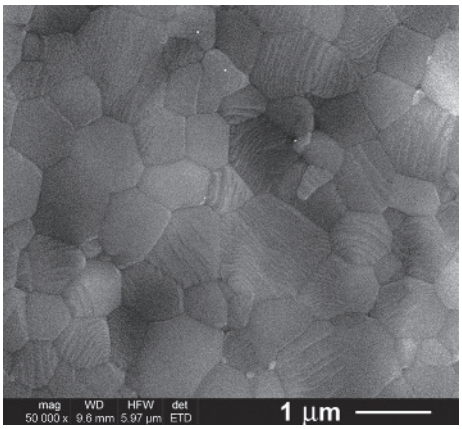
mag WD HFW det
50 000 x 9.6 mm 5.97 µm ETD
1 µm

(d)

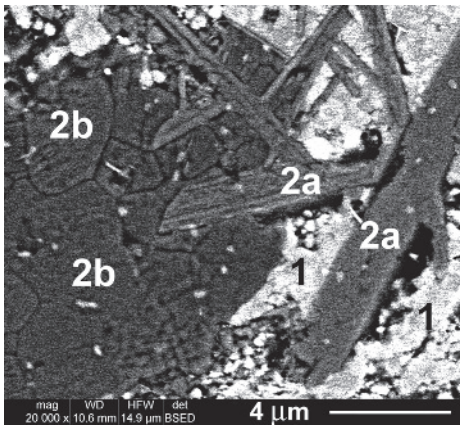
2b
2a
2a
2b
1
1
mag WD HFW det
20 000 x 10.6 mm 14.9 µm BSED
4 µm

(e)

specimen with built-in Ti vacancies, also sintered at 1200 °C. A general view of sample D sintered at 1300 °C and described by the same nominal formula indicates the single-phase composition of this ceramic (Figure 1.6(f)).

Values of the Ba:Ti ratio in several zones marked with numbers that correspond to each phase on FE-SEM images were determined by quantitative EDX analyses. Any possible difference in cerium amount in the samples sintered at 1200 °C in comparison with those sintered at 1300 °C is hard to determine in the regions corresponding to the perovskite phase. At this doping level, the results are not relevant since they are found in the margin of error of measurement. Moreover, because of overlapping of the strongest Ce line (Ce$L\alpha_{1,2}$) by the Ba$L\beta_{1,4}$ line, an accurate estimation of small cerium concentrations in barium titanate solid solutions becomes an even more difficult task. Given the high sensitivity of the Curie temperature value to very small amounts of Ce^{3+} incorporated on Ba sites, it is expected that dielectric measurements can provide a more realistic view in terms of dopant incorporation at different sintering temperatures in the investigated ceramic samples.

Regarding the charge compensation mechanism in perovskite phases, it is clear that exclusive compensation via a barium vacancy is very unlikely, since no barium-rich secondary phases were detected in any of our ceramics. Only in the single-phase ceramic sample D could one assume an exclusive compensation via Ti vacancies taking into account the starting formula and the lack of secondary phases. Based on the values of the Ba/Ti ratio estimated from quantitative EDX analyses, we were not able to find if the most likely compensating mechanism in the perovskite phase involves only Ti vacancies or an equal number of Ti and Ba vacancies in both ceramics sintered at 1200 °C (A and C), as well as in the ceramic sample without built-in compensating Ti vacancies (B) sintered at 1300 °C. This difficulty originates in the close values of the Ba/Ti ratio specific to the mentioned compensation mechanisms. Thus, if we assume an amount of 4 at% Ce^{3+} on Ba sites incorporated in the perovskite phase of both ceramics sintered at 1200 °C, compensation via exclusive Ti vacancies should involve a Ba/Ti ratio of ∼0.97 in the perovskite solid solution, while the mechanism involving equal numbers of barium and titanium vacancies should lead to a Ba/Ti ratio of ∼0.96. The capability of our equipment in providing very accurate quantitative results is not powerful enough to distinguish between them. We can only conclude that FE-SEM observations regarding the phase composition of the sintered specimens supported the XRD data.

FE-SEM investigations in the SE mode were carried out on polished cross-sections after thermal etching. The FE-SEM image of the ceramic sample A ($Ba_{0.95}Ce_{0.05}TiO_3$) sintered at 1200 °C/4 h shows a fine-grained, non-uniform, and porous microstructure, consisting of submicrometer grains (average grain size of 0.35 μm) with no well-marked grain boundaries and a significant amount of intergranular, interconnected porosity (Figure 1.7(a)). In some regions, these small grains exhibit an obvious aggregation tendency by neck formation, which indicates a rather incipient sintering stage. This explains the lower

Figure 1.7 *FE-SEM images in SE mode (a) to (d) and in BSE mode (e) on polished cross-sections after thermal etching of: (a), (b) $Ba_{0.95}Ce_{0.05}TiO_3$ and (c), (d) $Ba_{0.95}Ce_{0.05}Ti_{0.9875}(V''''_{Ti})_{0.0125}O_3$ ceramics, obtained after sintering in air at: (a), (c) 1200 °C/4 h and (b), (d) 1300 °C/4 h, respectively; (e) detail showing the morphology of polytitanate phases in the $Ba_{0.95}Ce_{0.05}TiO_3$ ceramic sintered at 1300 °C/4 h*

value of the relative density of only 74% determined for this specimen. Ceramic sample C ($Ba_{0.95}Ce_{0.05}Ti_{0.9875}(V_{Ti}''''')_{0.0125}O_3$), sintered in similar conditions, also exhibits a fine-grained microstructure (Figure 1.7(c)), but the microstructure is more homogeneous, the grain's shape and size is uniform, grain boundaries are well defined, and the intergranular porosity is significantly lower, which suggests that the presence of built-in V_{Ti}'''' as compensation defects exerts a favourable influence on the densification process. An almost similar average grain size of 0.33 μm and a relative density value of ∼87 % were determined for this sample. The densification process is more effective in the temperature range of 1200–1300 °C. Thus, the fine-grained ceramics with compositions described by both nominal formulae, which resulted after sintering at 1300 °C/4 h (B and D), show denser microstructures (Figure 1.7(b) and (d)) and significantly higher relative density values, of 83 and 95%, respectively. The $Ba_{0.95}Ce_{0.05}TiO_3$ sample (B) sintered at 1300 °C/4 h exhibits a non-homogeneous microstructure with bimodal grain size distribution, consisting of a lower amount of smaller grains of ∼0.29 μm randomly distributed into a matrix of polyhedral larger grains of ∼1.14 μm (Figure 1.7(b)). A residual intergranular porosity was still detected. As for the specimens sintered at 1200 °C, the beneficial effect on the densification induced by the presence of the built-in Ti vacancies is clearly revealed by the microstructure of the $Ba_{0.95}Ce_{0.05}Ti_{0.9875}(V_{Ti}''''')_{0.0125}O_3$ ceramic sample (D) sintered at 1300 °C. In this case, uniform grain growth took place, so that a homogeneous, almost pore-free matrix-like microstructure with unimodal grain size distribution and consisting of polyhedral grains (average grain size of 0.87 μm) with well-defined grain boundaries and almost perfect triple junctions was observed (Figure 1.7(d)).

A careful investigation of the secondary polytitanate phases with different Ba/Ti ratios was performed in order to find if they are somewhat different from a morphological point of view. The FE-SEM image in the BSE mode on polished and thermally etched cross-section of sample B indicated that the polytitanate phases exhibit dissimilar grain morphology. Thus, the darker gray polytitanate area with a higher Ti content (denoted 2b), whose Ba:Ti ratio of ∼1:4 seems to indicate the presence of $BaTi_4O_9$, represents an agglomerate of equiaxial grains, while the lighter shaded elongated areas (denoted 2a), with a lower Ba:Ti ratio (of ∼1:3), which according to the XRD pattern of this sample should correspond to $Ba_4Ti_{12}O_{27}$ (Figure 1.4(b)), show no structuring. Therefore, these unidimensionally extended and randomly oriented areas are actually individual grains with fibrous or rod-like morphology (Figure 1.7(e)), which sometimes are welded into bundles.

1.3 Dielectric Properties

The electrical measurements were performed on a parallel-plate capacitor configuration, by applying Pd–Ag electrodes on the polished surfaces of the sintered ceramic disks. The complex impedance in the frequency range of $2–10^6$ Hz and for temperatures of –150–160 °C was determined by using a dielectric spectrometer CONCEPT 40 Novocontrol Technologies.

Figure 1.8 (a) to (d) presents the temperature dependence of permittivity at a few selected frequencies, in the range of 1 Hz–1 MHz. All the samples show a well-defined frequency-independent maximum of permittivity assigned to the ferroelectric–paraelectric phase transition (Curie temperature T_C). A small frequency dispersion is observed only in the

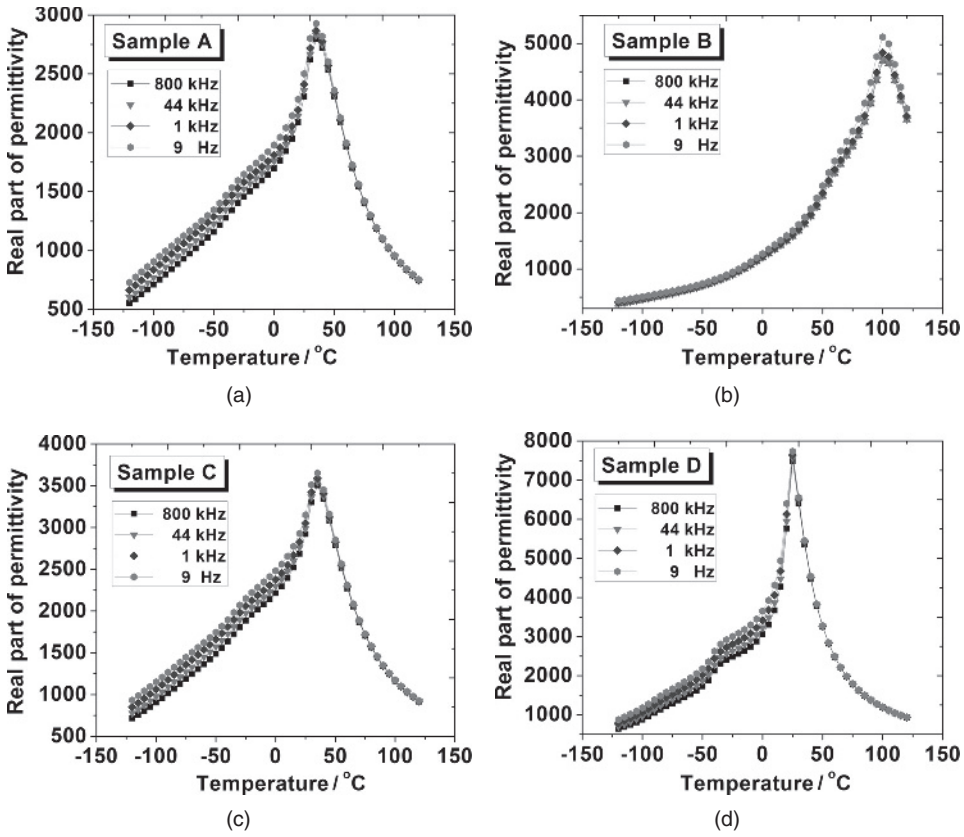

Figure 1.8 *Temperature dependence of the real part of the dielectric constant for: (a) sample A ($Ba_{0.95}Ce_{0.05}TiO_3$ sintered at 1200 °C/4 h); (b) sample B ($Ba_{0.95}Ce_{0.05}TiO_3$ sintered at 1300 °C/4 h); (c) sample C ($Ba_{0.95}Ce_{0.05}Ti_{0.9875}(V''''_{Ti})_{0.0125}O_3$ sintered at 1200 °C/4 h); and (d) sample D ($Ba_{0.95}Ce_{0.05}Ti_{0.9875}(V''''_{Ti})_{0.0125}O_3$ sintered at 1300 °C/4 h)*

ferroelectric phase for all the samples, with the exception of ceramic B (Figure 1.8(b)), while in the paraelectric state above T_C, the permittivity is almost frequency independent for all the ceramics.

For a better comparison of the dielectric data for all Ce-doped $BaTiO_3$ ceramics, the temperature dependence of the dielectric constant and tangent loss at a fixed frequency $f =$ 1 kHz are comparatively shown in Figure 1.9(a) and (b), respectively. The ceramics show good dielectric properties, with dielectric losses below 5% in the overall temperature range. In particular, the tangent loss values are significantly suppressed at temperatures above the Curie temperature T_C (Figure 1.9(b)). At the lowest temperature, the data revealed permittivity values slightly below 1000 for all of the ceramic samples. The ceramic with built-in titanium vacancies sintered at 1300 °C (sample D) presents the highest values of permittivity in the overall investigated temperature range, with a maximum at about ∼7720, by comparison with values of about ∼4910 (sample B), ∼3620 (sample C), and ∼2900 (sample A), at their corresponding ferroelectric–paraelectric transition temperatures (Figures 1.8

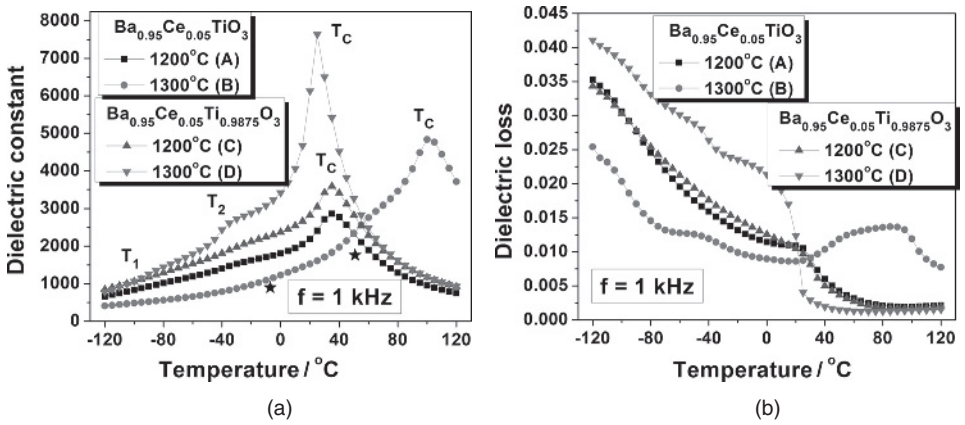

Figure 1.9 *Comparative representation of the temperature dependence of the real part of the dielectric constant and (a) tangent loss, tan δ and (b) for 5% Ce–$BaTiO_3$ ceramics at frequency f = 1 kHz*

and 1.9(a)). The particular high permittivity determined for this sample is most likely due to its peculiar microstructure, showing almost full densification (Figure 1.7(d)), while the lowest permittivity of the A sample is mainly caused by its highest porosity (Figure 1.7(a)).

The ferroelectric–paraelectric phase transitions are clearly evidenced by the maximum permittivity, indicating a sharper ferroelectric–paraelectric phase transition for the ceramics sintered at a higher temperature (1300 °C) and a slightly more diffuse permittivity maxima for the samples sintered at a lower temperature (1200 °C). The phase transition diffuseness is most likely favoured by the lower densification and smaller grain size. The Curie temperature T_C is in the range of 25–35 °C, with the exception of the $Ba_{0.95}Ce_{0.05}TiO_3$ sample (B), for which T_C is much higher (around ∼102 °C). This anomalous value is closer to the tetragonal–cubic phase transition temperature of undoped $BaTiO_3$ (110–120 °C) and confirms the pure tetragonal ferroelectric structure detected by XRD at room temperature, unlike the other sample (A) with a similar composition but sintered at a lower temperature, for which the mixture of cubic and tetragonal phases at room temperature is related to the proximity of the ferroelectric–paraelectric phase transition. However, one can observe that for both compositions sintered at a lower temperature (1200 °C), the Curie temperatures are slightly higher, of 36 and 35 °C for the ceramic samples A and C, respectively, by comparison with the value of 25 °C of specimen D, with built-in titanium vacancies, sintered at 1300 °C. According to Jing et al. [26], a T_C value of ∼40 °C is obtained for the composition with 4 at% Ce^{3+} solubilized on Ba sites in $BaTiO_3$, so we can assume that an almost similar Ce^{3+} content must have been incorporated in the perovskite phase of our ceramics A and C sintered at 1200 °C. This value of Ce^{3+} concentration is similar to the solubility limit ($x = 0.04$) at 1200 °C found by Makovec et al. [10] for cerium incorporation as Ce^{3+} on Ba sites. These results support the conclusion emphasized by XRD data and FE-SEM observations that, at a lower sintering temperature, not the whole nominal cerium content was incorporated in the corresponding perovskite solid solutions because of the internal oxidation of Ce^{3+}, leading to precipitation of small amounts of CeO_2.

Only the single-phase ceramic sample D, with built-in compensating defects and sintered at 1300 °C, shows the normal Curie temperature value reported by the literature data for an incorporation of 5 at% Ce^{3+} on Ba sites into the $BaTiO_3$ lattice [1, 11, 12, 31]. Consequently, only in this specimen does the composition of the perovskite solid solution seem to coincide with the $Ba_{0.95}Ce_{0.05}Ti_{0.9875}(V'''')_{0.0125}O_3$ nominal formula.

The features of the other structural phase transitions are not well defined in Figure 1.9(a). Values in the range of –25–40 °C were determined for the orthorhombic–tetragonal phase transition temperature T_1 for samples A, C, and D. Besides the significant decrease of the Curie temperature for Ce-doped compositions relative to undoped $BaTiO_3$, the additional shift of the orthorhombic–tetragonal phase transition temperature towards lower temperature values support the conclusions that for A, C, and D ceramics cerium was exclusively incorporated as Ce^{3+} on Ba sites into the perovskite lattice.

As in the case of the Curie temperature, one can observe that for both ceramics A and C sintered at a lower temperature (1200 °C), the values corresponding to the orthorhombic–tetragonal phase transition T_1 are slightly higher, of ∼ –25 °C, by comparison with the value of ∼ –39 °C determined for specimen D, proving once again that at 1200 °C not all the cerium content indicated by the nominal compositions was integrated in the perovskite lattice.

The rhombohedral–orthorhombic transition temperature T_2 was even more difficult to be observed. It was only detected from small anomalies of the derivative of permittivity versus temperature dependence. Values of about –93 and –91 °C for the A and D samples, respectively (similar to the ones of pure $BaTiO_3$), slightly higher for the C sample (–83 °C), and almost undetectable for the $Ba_{0.95}Ce_{0.05}TiO_3$ ceramic (B) sintered at a higher temperature were obtained for T_2. For the sample B, two anomalous features (indicated by star symbols in Figure 1.9(a)) at about –7 and 51 °C were observed besides the already mentioned Curie temperature $T_C = 102$ °C. They might be assigned to the rhombohedral–orthorhombic and orthorhombic–tetragonal transitions, respectively. However, if the anomaly at 51 °C is assigned to the orthorhombic–tetragonal phase transition, the room temperature symmetry should be predominantly orthorhombic and not tetragonal, as resulted from XRD analysis. However, for this composition, the XRD data were accurately fitted by using only the JCPDS file indexed for the tetragonal $BaTiO_3$ (i.e. JCPDS no. 05-0626), by comparison with any other JCPDS file corresponding to orthorhombic $BaTiO_3$. We concluded that the orthorhombic distortion in this Ce–$BaTiO_3$ specimen could be smaller or somewhat different from that of the pure $BaTiO_3$ orthorhombic state. Taking into account that the calculation of the structural parameters by XRD involves an averaging over about 10^4 unit cells, one can conclude that this investigation method is not sensitive enough to make a clear difference between the tetragonal and orthorhombic distortion in the case of such a solid solution and only the electrical measurements against the temperature are able to indicate the presence of the orthorhombic modification.

The anomalous behaviour of sample B relative to the Curie temperature value might be explained in terms of a significantly lower amount of Ce^{3+} ions replacing the host Ba^{2+} ions on their sites, rather than one corresponding to the nominal formula, in which a substitution degree of $x = 0.05$ (5 at%) on A sites of the ABO_3 perovskite lattice was considered. According to the dielectric data reported by Hwang and Han [11, 12], a concentration of only ∼2 at% cerium incorporated as Ce^{3+} on Ba^{2+} sites can determine such a high value for T_C. This means that the rest of the cerium should be oxidized and precipitated as CeO_2.

This is not supported by XRD analyses or by SEM investigations. On the other hand, if we assume a lower Ce^{3+} amount exclusively incorporated on Ba sites, it should also contribute to the concurrent lowering of the orthorhombic–tetragonal phase transition temperature T_1, specific to the incorporation of donor dopants in $BaTiO_3$. As already mentioned, even if in A and C specimens sintered at lower temperature (1200 °C) Ce^{3+} was not entirely incorporated in the perovskite phase according to the nominal formula, the amount of Ce^{3+} integrated on Ba sites clearly contributed to the decrease of the orthorhombic–tetragonal phase transition temperature, relative to pure $BaTiO_3$. Unlike these specimens, ceramic B shows an opposite evolution consisting of a significant increase in T_1. Therefore, the lower amount of Ce^{3+} incorporated on Ba sites cannot explain the abnormal increase of T_1 in sample B. The only reasonable explanation for this strange behavior is homovalent incorporation of a certain amount of cerium as Ce^{4+} on Ti^{4+} sites.

It is well known that the homovalent incorporation of cerium as Ce^{4+} on Ti^{4+} sites induces a much less pronounced decrease of the Curie temperature and a concurrent strong increase of the rhombohedral – orthorhombic (T_2) and orthorhombic–tetragonal (T_1) phase transition temperatures compared with those of ∼–90 and ∼5 °C, respectively, specific to pure barium titanate [27].

If considering that the anomaly at ∼51 °C detected in the ceramic B can be attributed to the orthorhombic–tetragonal phase transition, which is shifted towards much higher temperatures than in the case of undoped $BaTiO_3$ and taking into account the high sensitivity of T_1 to the Ce^{4+} incorporation on the Ti-sites [27], one can conclude that, for this sample, it is most likely that a significant amount of cerium was incorporated as Ce^{4+} on Ti^{4+} sites. This suggests that in ceramic sample B, a higher sintering temperature induces a further internal oxidation of Ce^{3+} to Ce^{4+}. Unlike the samples sintered at lower temperatures, in this case Ce^{4+} is not expelled as CeO_2 precipitate, but instead replaces Ti^{4+} in the host lattice. This process is accompanied by exclusive segregation of Ti-rich precipitates with different Ba/Ti ratios, as XRD, FE-SEM, and EDX results indicated. Therefore, formation of polytitanate phases with various Ba/Ti ratios in the $Ba_{0.95}Ce_{0.05}TiO_3$ sample (B) sintered at 1300 °C might be determined by two concurrent phenomena: (i) predominant incorporation of cerium as Ce^{4+} on Ti^{4+} sites, which implies expelling from the perovskite lattice of a Ti^{4+} an amount equal to the amount of Ce^{4+} integrated on the Ti sites and the consequent enrichment in Ba of the perovskite phase and (ii) a charge compensation mechanism via Ti vacancies of the remaining Ce^{3+} incorporated on Ba sites, which should also lead to a supplementary segregation of Ti-rich secondary phases. It is hard to quantify the contribution of each of these phenomena to the appearance of the Ti-rich secondary phases, but it seems logical to assume that the segregation of polytitanates due to Ce^{4+} incorporation on Ti sites prevails over any charge compensation mechanism induced by a low content of Ce^{3+} (significantly lower than that stipulated by the nominal formula) incorporated on Ba sites, which might induce the same effect.

In contrast, sample D sintered in similar conditions but with built-in Ti vacancies is single phase, which means that no internal oxidation of Ce^{3+} occurred at 1300 °C. Moreover, it behaves normally from an electrical point of view, with a significant decrease of T_C and T_1 with the increase of Ce^{3+} content. Taking into account these aspects, one can conclude that the lack of compensating defects in sample B prevents the entire accommodation of Ce^{3+} on Ba sites, while the higher efficiency of *B*-site diffusion induced by the higher sintering

temperature somehow facilitates a preferential incorporation of the solute as Ce^{4+} on Ti sites. The origin of this phenomenon is unclear and is still under investigation.

On the other hand, if we assume an exclusive incorporation of cerium as Ce^{4+} on Ti sites, then, according to data reported by Zhang et al. [28], the Curie temperature should be even higher, of ∼120 °C. In fact, Zhang et al. [28] are the only ones to report the electrical behavior of $BaTi_{0.95}Ce_{0.05}O_3$ ceramic. A value T_1 of 77 °C for the orthorhombic–tetragonal phase transition temperature was also found [28]. Their results converge with those reported by Hwang and Han [11], where a T_C of 135 °C, practically composition-independent for Ce^{4+} amounts below 3 at% and a T_1 value of 70 °C for $BaTi_{0.97}Ce_{0.03}O_3$ ceramic, were found. A steeper decrease of T_C with the increase of Ce^{4+} amount integrated on Ti sites was reported by Jing et al. [27] and Ang et al. [30], who found for the $BaTi_{0.98}Ce_{0.02}TiO_3$ composition a T_C value of 118 °C and a T_1 value of 52 °C, while for the composition $BaTi_{0.94}Ce_{0.06}TiO_3$ a pinched phase transition at 108 °C was detected. Therefore, even if we refer to the results of Jing et al. [27], an entire Ce^{4+} homovalent incorporation of Ti^{4+} sites should involve a higher Curie temperature value than that (of 102 °C) already determined for sample B. Consequently, it was found that in ceramic specimen B a mixed incorporation involving both Ce^{3+} on Ba sites and of Ce^{4+} on Ti sites was most likely to take place. Comparing our results with the literature data regarding the values of the phase transition temperatures in Ce^{3+}- and Ce^{4+}-doped $BaTiO_3$, it seems that in our $Ba_{0.95}Ce_{0.05}TiO_3$ ceramic sintered at 1300 °C, a smaller amount of Ce^{3+} enters on Ba sites concurrently with a higher content of Ce^{4+}, which replaces Ti^{4+} in the host $BaTiO_3$ lattice. Thus, homovalent substitution of Ti^{4+} by Ce^{4+} is responsible for the shift of the rhombohedral–orthorhombic and orthorhombic–tetragonal phase transition temperatures towards higher temperature values, while the decrease of the Curie temperature is mainly induced by Ce^{3+} incorporated on Ba sites.

However, the orthorhombic–tetragonal phase transition temperature T_1 represents in this case the resultant between two opposite evolutions, that is a major increasing trend induced by Ce^{4+} incorporated on Ti sites, but also a certain contribution of Ce^{3+} incorporated on Ba sites to lowering this temperature. Based on the literature data [1, 11, 25–31], we approximated that a solid solution with 2 at% of Ce^{3+} on Ba sites and 3 at% Ce^{4+} on Ti sites might present T_C and T_1 values close to those found for this peculiar ceramic. As in the case of both ceramics A and C sintered at 1200 °C, we were not able to accurately estimate the composition corresponding to the perovskite phase in the sample B. Only for the $Ba_{0.95}Ce_{0.05}Ti_{0.9875}(V_{Ti}'''')_{0.0125}O_3$ single-phase ceramic sintered at a high temperature (1300 °C) does the experimental evidence allow a claim to be made without doubt of charge compensation via Ti vacancies. For other investigated samples, based on dielectric data versus temperature, we were only able to establish the site occupancy of the solute in the host perovsite lattice of $BaTiO_3$.

The mixed incorporation of both Ce^{3+} on Ba sites and Ce^{4+} on Ti sites seems to be in disagreement with the results of Hwang and Han [11], where no anomalous electrical behavior for the ceramics described by the $Ba_{1-x}Ce_xTiO_3$ formula was reported. Unlike our ceramic sample B, a T_C value of 26 °C and a T_1 value of –36 °C were found, which proves the exclusive incorporation of cerium as Ce^{3+} on Ba sites for the $Ba_{0.95}Ce_{0.05}TiO_3$ sample sintered in air at 1350 °C/5 h. No secondary phases were detected in the mentioned ceramic and, in a later work [12], they claimed the occurrence of a mixed compensation mechanism

involving an equal number of V''_{Ba} and V''''_{Ti} for the effective positive extra charge induced by the donor dopant.

Therefore, further experiments aimed to reveal whether such abnormal behaviour might also occur for ceramics with similar $Ba_{0.95}Ce_{0.05}TiO_3$ nominal composition prepared by other wet-chemical methods and sintered in similar conditions.

The mixed incorporation of the cerium solute in the ceramic sample B is also supported by the values of the structural parameters calculated from the XRD data (Table 1.2). Thereby, the higher values of the lattice parameters for the specimen B sintered at 1300 °C compared to those specific to the sample A, with similar composition but sintered at a lower temperature (1200 °C), can be explained in terms of a predominant replacement of the smaller Ti^{4+} ions (ionic radius of 0.605Å [36]) with the slightly larger Ce^{4+} cations (ionic radius of 0.87Å [36]). The shift of the main diffraction peaks corresponding to the perovskite phase towards lower values of the diffraction angle, as indicated in Figure 1.4(a), also support the idea that the influence of homovalent incorporation of Ce^{4+} on Ti^{4+} sites prevails in ceramic B.

Empirical parameters are currently used to characterize the ferroelectric behavior. The dielectric constant versus temperature at the higher temperature above T_C follows the Curie–Weiss law:

$$\frac{1}{\varepsilon'} = \frac{T - T_0}{C} (T > T_C) \tag{1.6}$$

where T_0 is the Curie–Weiss temperature and C is the Curie constant. Figure 1.10 shows the reciprocal dielectric constant as a function of temperature at 1 kHz, which are well fitted by the Curie–Weiss law. The permittivity follows the Curie–Weiss law above T_C for all the samples with the parameters (T_0 and C) shown in Table 1.3.

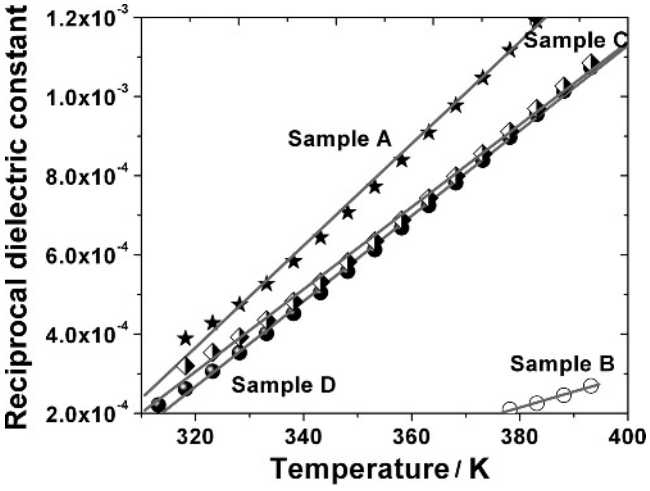

Figure 1.10 *Reciprocal permittivity as a function of temperature at 1 kHz for 5% Ce-doped $BaTiO_3$ and fits by the Curie–Weiss law*

Table 1.3 *Fitting parameters (T_0 and C) of the Curie–Weiss law and ε_{max} and T_C determined at the frequency f = 1 kHz for the 5% Ce-doped $BaTiO_3$*

Sample	ε_{max}	T_C (°C)	T_0 (°C)	C (K)
A	2868	36	18	0.8×10^5
B	4838	102	53	2.5×10^5
C	3590	35	17	1.0×10^5
D	7640	25	22	0.9×10^5

The Curie–Weiss temperature increases by increasing the sintering temperature. The Curie constant is very similar (in the range of (0.8–1.0) × 10^5 K), for the A, C, and D samples, while a 2.5 times larger value of ∼2.5 × 10^5 K is obtained for the B sample (Table 1.3). The higher Curie constant value is related to a stronger polar long-range order character (stronger ferroelectricity) of this ceramic, which correlates well with the high Curie temperature and with its higher structural polar distortion, which resulted from a lower level of Ce^{3+} incorporation on Ba sites and a predominant incorporation of Ce^{4+} on Ti sites. The dielectric data and the Curie–Weiss analysis sustain the results of the structural calculations, which indicated a high polar distortion at room temperature in this sample.

1.4 Raman Investigation

In order to emphasize the evolution of the phase transitions versus temperature and to explain the dissimilar Curie temperature values obtained for the ceramic samples sintered at 1300 °C/4 h but described by different nominal formula, temperature-dependent Raman spectroscopy was used as a complementary investigation method.

Raman spectra were obtained with a T64000 Raman system (Horiba/Jobin-Yvon, Villeneuve d'Ascq, France) working in micro-Raman mode and using a 514.5 nm Ar ion laser (Coherent Innova 400, Coherent, Santa Clara, CA, USA) as the excitation source. The laser light was focused on the sample surface by means of a long working distance ×50 objective lens with a numerical aperture NA = 0.5 (Olympus, Tokyo, Japan). The nominal power was set either to 20 mW or to 7 mW, depending of the temperature sensitivity of the sample. Spectra were collected in a true backscattering geometry with the aid of a liquid nitrogen-cooled charged coupled device (CCD) camera. Temperature-dependent (in situ) Raman experiments were performed by means of a Linkam THMS600 heating–cooling stage (Linkam, Tadworth, UK). Spectra were collected in the range of –190–110 °C in a triple subtractive configuration, in order to allow measurements in the low-wavenumber region (∼50 cm^{-1}).

Figure 1.11 reports temperature-dependent Raman spectra of the previously mentioned B and D ceramic samples resulting after sintering at 1300 °C. For the ceramic sample B, without compensating defects, the Raman spectra clearly show a rhombohedral (R) modification at low temperatures (Figure 1.11(a)). This is indicated by the presence of the peaks at low wavenumbers (161 and 196 cm^{-1}) and especially by a distinct mode at ∼490 cm^{-1}, which is only present in the R phase [39, 40]. These features seem to persist until –50 °C (Figure 1.11(a)). At higher temperatures, the damping of the mode at 490 cm^{-1} indicates the

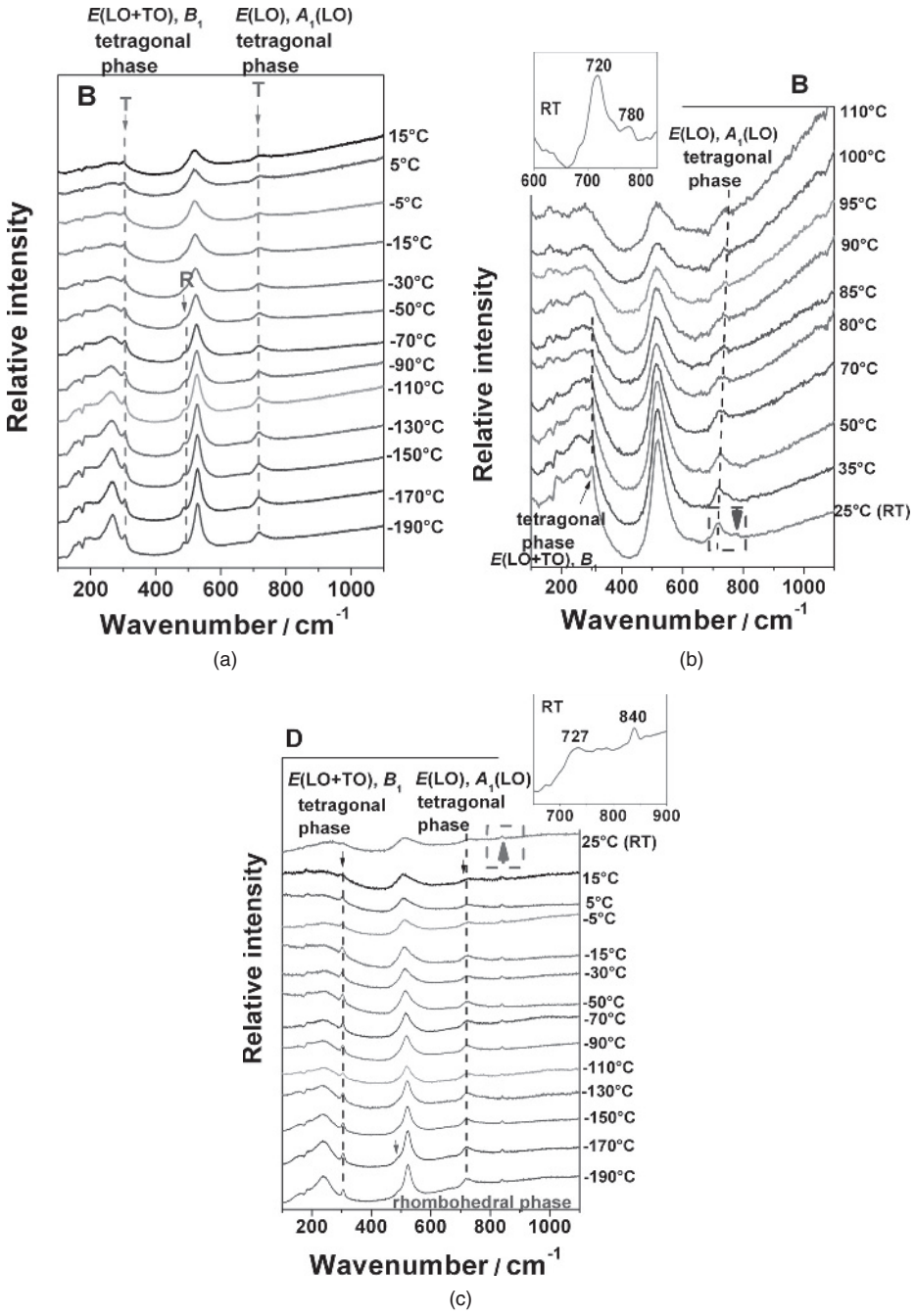

Figure 1.11 *Evolution of Raman spectra versus temperature for the ceramic samples sintered at 1300 °C/4 h: (a) $Ba_{0.95}Ce_{0.05}TiO_3$ sample (B) in the temperature range of –190–15 °C; (b) sample B in the temperature range of 25–110 °C – inset: detail (dashed rectangle) of the wavenumber region 600–850 cm^{-1}; (c) $Ba_{0.95}Ce_{0.05}Ti_{0.9875}(V''''_{Ti})_{0.0125}O_3$ sample (D) in the temperature range of –190–25 °C – inset: detail (dashed rectangle) of the wavenumber region 650–900 cm^{-1}.*

transition from rhombohedral (R) to orthorhombic (O) symmetry. However, the persistence of the twin peaks at 160 and 183 cm^{-1} shows that a certain residual rhombohedral order still exists, so that in the temperature range of –50–50 °C a mixture of O and R modifications is more appropriate (Figure 1.11(a and (b)). This observation is in agreement with the results of the dielectric data (Figure 1.8), in which the room temperature state is located between the two anomalies at –7 and 51 °C, corresponding to the R–O and O–T phase transitions, respectively. The interference dip at 176 cm^{-1}, together with the "silent" mode at 302 cm^{-1} and the mode at 715 cm^{-1} represent clear indications that long-range ferroelectric order is present in the lattice [37, 38] at room temperature.

Transition to the cubic (C) paraelectric phase seems to occur above 100 °C, as indicated by the gradual disappearance of the "silent" mode at 302 cm^{-1} and the decrease in intensity of the mode at 715 cm^{-1}, both specific to the tetragonal phase. A Curie temperature of 102 °C was also detected by the permittivity versus temperature data. The evolution of the main features in the Raman spectra recorded at various temperatures suggests a diffuse character of the phase transition, as in relaxor ferroelectrics. The persistence of the Raman spectrum also in the C paraelectric phase above 100 °C is due to the presence of small distortions in the short-range polar nanoregions (PNRs), producing Raman activity even if it is forbidden by the long-range cubic crystalline structure [39]. Taking into account these observations, it is clear that the ceramic sample B sintered at 1300 °C/4 h is in its polar/ferroelectric state at room temperature. These results are in good agreement with both the structural parameters calculated from the XRD data and the Curie temperature estimated from the dielectric study. In the room temperature spectrum of this sample an additional small peak is noticed at 780 cm^{-1}, indicated by the arrow in Figure 1.11(b) and better pointed out by the inset placed in the top-left corner of the same figure. This small peak is generally related to a *B*-site substitution in $BaTiO_3$-based solid solutions [37, 40]. The presence of this peak supports our assumption regarding the predominant incorporation of cerium as Ce^{4+} on titanium sites in the perovskite lattice of the $Ba_{0.95}Ce_{0.05}TiO_3$ ceramic sintered at 1300 °C.

Unlike this case, in the $Ba_{0.95}Ce_{0.05}Ti_{0.9875}(V_{Ti}'''')_{0.0125}O_3$ specimen sintered in similar conditions, the rhombohedral distortion appears at much lower temperatures (< –150 °C) if only the presence of the mode located at 490 cm^{-1} is considered (Figure 1.11(c)).

Concerning the tetragonal modification, this is still identified at 15 °C by means of the "silent mode", but is missing at higher temperatures. This result is consistent with the dielectric properties, which revealed that for this composition the Curie temperature coincides with the room temperature. Another interesting feature in the Raman spectra of this ceramic is the presence of a small peak located at ∼ 840 cm^{-1} (indicated by the arrow in Figure 1.11(c)), related to the substitution on the *A* sites of the perovskite lattice). This suggests that in this case the entire dopant amount is integrated as Ce^{3+} on Ba^{2+} sites. This mode is better visualized in the inset placed in the top-right corner of Figure 1.11(c). It is worth mentioning that this mode was not observed in the Raman spectra of the sample B described by the nominal formula $Ba_{0.95}Ce_{0.05}TiO_3$, most likely because of the significantly smaller amount of cerium incorporated on barium sites [41, 42].

1.5 Conclusions

Nanopowders of 5% Ce-doped $BaTiO_3$ with two nominal compositions involving the lack and the presence of Ti vacancies as charge compensating defects and described by the

nominal formulae $Ba_{0.95}Ce_{0.05}TiO_3$ and $Ba_{0.95}Ce_{0.05}Ti_{0.9875}(V_{Ti}^{''''})_{0.0125}O_3$ were prepared by the modified Pechini method. From these powders ceramic samples were obtained after sintering in air at two temperatures, 1200 °C/4 h and 1300 °C/4 h, respectively. The phase purity, structural parameters, and microstructural characteristics were investigated.

Only the specimen with built-in titanium vacancies sintered at 1300 °C showed a single-phase composition. Internal oxidation of Ce^{3+} to Ce^{4+} takes place in both samples sintered at 1200 °C, as well as in the specimen without compensating defects sintered at 1300 °C. As a result, small amounts of CeO_2 precipitate were detected for the ceramics sintered at 1200 °C, while a predominant homovalent incorporation of cerium as Ce^{4+} on Ti sites was found in the specimen without Ti vacancies sintered at 1300 °C. The Ce^{3+} oxidation is accompanied by segregation of Ti-rich secondary phases with various Ba/Ti ratios, as revealed by XRD and FE-SEM investigations. The values of the structural parameters calculated from XRD data, as well as the values of the phase transition temperatures indicated by dielectric measurements versus temperature support the assumption of an exclusive but incomplete incorporation (relative to the nominal formula) of the cerium as Ce^{3+} on the Ba site into a perovskite lattice for both ceramics sintered at 1200 °C and of a mixed incorporation of the cerium, mainly as Ce^{4+} on Ti sites, but to a lesser extent also as Ce^{3+} on Ba sites, in the case of the specimen without Ti vacancies and sintered at 1300 °C.

All the ceramics investigated showed good dielectric properties characterized by low losses ($\tan \delta < 5\%$) and a high dielectric constant of 3000–8000 at their corresponding transition temperatures. Sharp ferroelectric–paraelectric phase transitions without a diffuse character and no apparent relaxor properties were determined.

Temperature-dependent Raman analyses sustain the XRD data and the results of the dielectric measurements, proving the mixed incorporation mechanism of cerium, with a predominant homovalent $Ce^{4+} \leftrightarrow Ti^{4+}$ substitution in the ceramic sample without built-in Ti vacancies, sintered at 1300 °C/4 h.

Acknowledgments

The financial support of the Romanian CNCS-UEFISCDI Projects No. PN-II-ID-PCE-2011-3-0668 and PN-II-PT-PCCA-2013-4-0470, as well as collaboration within COST MP0904 Action SIMUFER: "Single- and multiphase ferroics and multiferroics with restricted geometries", are highly acknowledged. Raman measurements were performed in the frame of the Croatian Ministry of Science Education and Sport Project, "Physics and applications of nanostructures and bulk matter", No. 098-0982904-2898.

References

(1) Hennings, D.F.K., Schreinemacher, B., and Schreinemacher, H. (1994) High-permittivity dielectric ceramics with high endurance. *Journal of the European Ceramic Society*, **13**, 81–88.

(2) Morrison, F.D., Sinclair, D.C., Skakle, J.M.S., and West, A.R. (1998) Novel doping mechanism for very-high-permittivity barium titanate ceramics. *Journal of the American Ceramic Society*, **81**, 1957–1960.

(3) Saburi, O. (1961) Semiconducting bodies in the family of barium titanates. *Journal of the American Ceramic Society*, **44**, 54–63.
(4) Jonker, G.H. (1964) Some aspects of semiconducting barium titanate. *Solid State Electronics*, **7**, 895–903.
(5) Drofenik, M., Popovic, A., and Kolar, D. (1984) Grain growth and related effects in doped $BaTiO_3$. *American Ceramic Society Bulletin*, **63**, 702–704.
(6) Desu, S.B., and Payne, D. (1990) Interfacial segregation in pervoskites: III, microstructure and electrical properties. *Journal of the American Ceramic Society*, **73**, 3407–3415.
(7) Kolar, D., Guha, J.P., and Buh, M. (1972) Ceramic and dielectric properties of selected compositions in the BaO-TiO_2-CeO_2 system. *Proceedings of the.British Ceramic Society*, **23**, 152–158.
(8) Roth, R.S., Negas, T., Parker, H.S., et al. (1977) Crystal chemistry of cerium titanates, tantalates and niobates. *Materials Research Bulletin*, **12**, 1173–1182.
(9) Itakura, G., Iguchi, T., and Kuroda, T. (1985) Ceramic dielectric materials with high dielectric constant for multilayer ceramic capacitors. *Natl Tech. Rep.* (Jpn), **31**, 145–156.
(10) Makovec, D., Samardžija, Z., and Kolar, D. (1996) Solid solubility of cerium in $BaTiO_3$. *Journal of Solid State Chemistry*, **123**, 30–38.
(11) Hwang, J.H. and Han, Y.H. (2000) Dielectric properties of $(Ba_{1-x}Ce_x)TiO_3$. *Japanese Journal of Applied Physics*, **39**, 2701–2704.
(12) Hwang, J.H. and Han, Y.H. (2001) Electrical properties of cerium-doped $BaTiO_3$. *Journal of the American Ceramic Society*, **84**, 1750–1754.
(13) Makovec, D., Samardžija, Z., and Kolar, D. (1993) Incorporation of cerium into the $BaTiO_3$ lattice, in *Proceedings of the Third European Ceramic Society Conference*, edited by P. Durán and J.P. Fernández, Faenza Editrice Ibérica S.L., Faenza, vol. 1, pp. 961–966.
(14) Guha, J.P. and Kolar, D. (1973) Subsolidus equilibria in the system BaO–CeO_2–TiO_2. *Journal of the American Ceramic Society*, **56**, 5–6.
(15) Chan, N.H. and Smyth, D.M. (1984) Defect chemistry of donor-doped $BaTiO_3$. *Journal of the American Ceramic Society*, **67**, 285–288.
(16) Kröger, F.A. and Vink, H.J. (1956) Relations between the concentrations of imperfections in crystalline solids, in *Solid State Physics*, edited by F. Seitz and D. Turnbull, Academic Press, New York, vol. 3, pp. 307–435.
(17) Lewis, C.V. and Catlow, C.R.A. (1986) Defect studies of doped and undoped barium titanate using computer simulation techniques. *Journal of Physics and Chemistry of Solids*, **47**, 89–97.
(18) Tien, T.Y. and Hummel, F.A. (1967) Solid solutions in the system.$SrTiO_3$–(La_2O_3:3TiO_2). *Transactions of the.British Ceramic Society*, **66**, 233–245.
(19) Hennings, D. (1971) The range of existence of perovskite phases in the system PbO–TiO_2–La_2O_3. *Materials Research Bulletin*, **6**, 329–339.
(20) Daniels, J., Härdtl, K.H., Hennings, D., and Wernicke, R. (1976) Defect chemistry and electrical conductivity of doped barium titanate ceramics. *Philips Research Reports*, **31**, 487–559.
(21) Chan, N.H., Harmer, M.P., and Smyth, D.M. (1986) Compensating defects in highly donor-doped $BaTiO_3$. *Journal of the American Ceramic Society*, **69**, 507–510.

(22) Jonker, G.H. and Havinga, E.E. (1982) The influence of foreign ions on the crystal lattice of $BaTiO_3$. *Materials Research Bulletin*, **17**, 345–350.
(23) Ianculescu, A., Mocanu, Z.V., Curecheriu, L.P., et al. (2011) Dielectric and tunability properties of La-doped $BaTiO_3$ ceramics. *Journal of Alloys and Compounds*, **509**, 10040–10049.
(24) Wang, L., Sakka, Y., and Shao, Y. (2010) Coexistence of A- and B-site vacancy compensation in La-doped $Sr_{1-x}Ba_xTiO_3$. *Journal of the American Ceramic Society*, **93**, 2903–2908.
(25) Ang, C., Yu, Z., Jing, Z., et al. (1997) Synthesis and characterization of $Ba(Ti_{1-x}Ce_x)O_3$ ceramics. *Journal of the European Ceramic Sociey*, **17**, 1217–1221.
(26) Jing, Z., Yu, Z., and Ang, C. (2002) Crystalline structure and dielectric behavior of $(Ce,Ba)TiO_3$ ceramics. *Journal of Materials Research*, **17**, 2787–2793.
(27) Jing, Z., Yu, Z., and Ang, C. (2003) Crystalline structure and dielectric properties of $Ba(Ti_{1-y}Ce_y)O_3$. *Journal of Materials Science*, **38**, 1057–1061.
(28) Zhang, Y., Sun, X., and Lu, D. (2006) Effects of cerium doping at Ti sites and europium doping at Ba sites on dielectric properties of $BaTiO_3$ ceramics. *Chem. Res. Chinese U.*, **22**, 515–519.
(29) Yu, Z., Ang, C., Jing, Z., et al. (1997) Dielectric properties of Ba(Ti, Ce)O_3 from 10^2 to 10^5 Hz in the temperature range 85–700 K. *Journal of Physics: Condensed Matter*, **9**, 3081–3088.
(30) Ang, C., Yu, Z., and Jing, Z. (2002) Ferroelectric relaxor Ba(Ti,Ce)O_3. *Journal of Physics: Condensed Matter*, **14**, 8901–8912.
(31) Klassens, H.A. and Philips, N.V. (1949) $BaTiO_3$–CeO_2 dielectric composition, German Patent No. 810 047.
(32) Yasmin, S., Choudhury, S., Hakim, M.A., et al. (2011) Effect of cerium doping on microstructure and dielectric properties of $BaTiO_3$ ceramics. *Journal of Materials Science and Technology*, **27**, 759–763.
(33) Cernea, M, Monereau, O., Llewellyn, P., et al. (2006) Sol–gel synthesis and characterization of Ce-doped- $BaTiO_3$. *Journal of the European Ceramic Society*, **26**, 3241–3246.
(34) Pechini, M.P. (1967) Method of preparing lead and alkaline earth titanates and niobates and coating method using the same for a capacitor, US Patent No. 3 330 697.
(35) Makovec, D. and Kolar, D. (1997) Internal oxidation of Ce^{3+}–$BaTiO_3$ solid solutions. *Journal of the American Ceramic Society*, **80**, 45–52.
(36) Shannon, R.D. (1976) Revised effective ionic radii and systematic studies of interatomic distances in halides and chalcogenides. *Acta Crystallographica A*, **32**, 751–767.
(37) Farhi, R., El Marssi, M., Simon, A., and Ravez, J. (1999) A Raman and dielectric study of ferroelectric $Ba(Ti_{1-x}Zr_x)O_3$ ceramics. *European Physical Journal B*, **9**, 599–604.
(38) Miao, S., Pokorny, J., Pasha, U.M., et al. (2009) Polar order and diffuse scatter in $Ba(Ti_{1-x}Zr_x)O_3$ ceramics. *Journal of Applied Physics*, **106**, art. no. 114111.
(39) Buscaglia, V., Buscaglia, M.T., Viviani, M., et al. (2005) Raman and AFM piezoresponse study of dense $BaTiO_3$ nanocrystalline ceramics. *Journal of the European Ceramic Society*, **25**, 3059–3062.

(40) Deluca, M., Vasilescu, C.A., Ianculescu, A.C., et al. (2012) Investigation of the composition-dependent properties of $BaTi_{1-x}Zr_xO_3$ ceramics prepared by the modified Pechini method. *Journal of the European Ceramic Society*, **32**, 3551–3566.
(41) Lu, D.Y., Sun, X.Y., and Toda, M. (2007) A novel high-*k* "Y5V" barium titanate ceramics co-doped with lanthanum and cerium. *Journal of Physics and Chemistry of Solids*, **68**, 650–664.
(42) Curecheriu, L.P., Deluca, M., Mocanu, Z.V., et al. (2013) Investigation of the ferroelectric–relaxor crossover in Ce-doped $BaTiO_3$ ceramics by impedance spectroscopy and Raman study. *Phase Transitions*, **86**, 703–714.